FABRICATION OF PLASMONIC NANOSTRUCTURES WITH ELECTRON BEAM INDUCED DEPOSITION

Thesis committee members:

prof. dr. J. Brugger	EPFL
prof. dr. M. C. Elwenspoek	Universiteit Twente
prof. dr. J. L. Herek	Universiteit Twente
prof. dr. P. Kruit	Tecnische Universiteit Delft
prof. dr. J. G. Rivas	Tecnische Universiteit Eindhoven
prof. dr. W. L. Vos	Universiteit Twente

Paranimfen:

A. Opheij
B. le Feber

This work was carried out at:
NanoOptics Group,
FOM Institute AMOLF
Science Park 104, 1098 XG Amsterdam, The Netherlands,
where a limited number of copies of this thesis is available.

Cover designed by Nur Acar
Printed by Wöhrmann Print Service, Zutphen, The Netherlands
ISBN: 978-90-77209-70-7

FABRICATION OF PLASMONIC NANOSTRUCTURES WITH ELECTRON BEAM INDUCED DEPOSITION

DISSERTATION

to obtain the degree of doctor at the University of Twente, on the
authority of the rector magnificus, prof.dr. H. Brinksma, on account of
the decision of the graduation committee, to be publicly defended on
Thursday 25 April 2013 at 12:45 hrs

by

Hakkı Acar
born in Ankara, Turkey

This dissertation has been approved by:
prof. dr. L. Kuipers

This work is a part of the research program of the Stichting voor Fundamenteel Onderzoek der Materie (FOM) which is financially supported by the Nederlandse organisatie voor Wetenschappelijk Onderzoek (NWO). The program is co-financed by FEI Company

بِسْمِ اللَّـهِ الرَّحْمَنِ الرَّحِيمِ

وَمَا تَوْفِيقِي إِلاَّ بِاللَّـهِ عَلَيْهِ تَوَكَّلْتُ وَإِلَيْهِ أُنِيبُ

Contents

1 Introduction **7**

1.1 General introduction 8

1.2 Outline of this thesis 10

2 Basics of EBID **13**

2.1 Introduction 14

2.2 History 14

2.3 Fundamentals of EBID 16

2.3.1 Main principle 16

2.3.2 Instrumental components 16

2.3.3 Precursor-solid interactions 19

2.3.4 Electron-substrate interaction 21

2.3.5 Electron-precursor interaction 22

2.4 Silica deposition with EBID 23

2.5 Conclusion 24

3 Dispersive ground plane core-shell type optical monopole antennas **25**

3.1 Introduction 26

3.2 Method 26

3.3 Measurement with the angle-resolved cathodoluminescence 27

3.4 Simulation of antenna properties 31

3.4.1 Finite element modeling 31

3.4.2 Building the model for the ground plane nanoantenna 32

3.5 Comparison of the measurement with the calculation 33

3.5.1 RF vs. nanoantenna in terms of the number of lobes 35

3.6 Effective index calculation of the nanoantennas 38
3.7 Conclusion 38

4 Fabrication of helical nanoantennas with electron beam induced deposition 41
4.1 Introduction 42
4.2 Method 44
    4.2.1 Nanostructuring of the helix array 45
    4.2.2 The parameters and effects on deposition 46
4.3 Conclusions 50

5 Optical activity of a chiral nanoantenna array 53
5.1 Introduction 54
5.2 Optical activity and circular dichroism 55
5.3 Results and discussion 57
    5.3.1 Experimental results 58
    5.3.2 Numerical calculations and comparison with the measurements 59
5.4 Conclusion 62
5.A Appendix: derivation of the optical rotation equation 5.2.0.1 64
5.B Appendix: derivation of the equation 5.2.0.4 66

6 Loaded plasmonic split-wire nanoantennas 67
6.1 Introduction 68
6.2 Method 68
6.3 Results and discussion 72
6.4 Conclusion 76

References 77

Summary 96

Samenvatting 98

Acknowledgements 100

Chapter 1

Introduction

The impact of development in nanoscience and nanotechnology is briefly discussed from the perspective of nanophotonics. The central aim of this thesis is elucidated by highlighting the strong connection between advanced nanofabrication and nanophotonics. The contents of the thesis is briefly introduced.

1.1 General introduction

Nanophotonics can be described as *"the study optical phenomena and techniques on the nanometer scale, that is, near or beyond the diffraction limit of light"* [1]. In other words nanophotonics involves the light-matter interaction related investigations that take place on length scales well below those of classical ray optics. The 'matter' is one of the most important factor in this phenomena. To understand and control the behavior of light on a (deep) subwavelength scale requires artificial materials engineered on a nanometer scale. Nanophotonics research has therefore emerged in the last decade as a result of the progress in advanced nanofabrication.

For example let us consider controlling of light with dielectric periodic structures [2]: in 1887 controlling the propagation of light with a 1D periodic stack was proposed by Rayleigh [3]. The first experimental demonstrations with 2D and 3D periodic dielectric structures (photonic crystals) took place in the late 1990s requiring nanometer precision in the fabrication [4, 5, 6] inspired by vast amount of theoretical and numerical works. [7, 8, 9, 10, 11]

Similarly, plasmonics can be considered as one of the main subfields of nanophotonics. It derives its potential of the unique optical properties of surface plasmon polaritons (SPPs): electromagnetic excitations that propagate along the interface between a metal and a dielectric [12, 13]. Whereas localized plasmons were already studied by Mie [14] in 1907 on small metal particles, even though he didn't use this terminology, SPPs on flat surfaces were discovered in 1957 by Ritchie [15]. The amount SPP related experimental and application researches really took off in the 1980s. In these studies electric field enhancement close to the metallic nanostructures was exploited for surface enhanced raman scattering (SERS) [16, 17, 18]. Although, the first applications started to emerge in the early 1980s, applied and pure optics related SPP studies got underway in the late nineties. Extraordinary transmission through subwavelength holes [19, 20], near- and far-field studies of SPP propagation on thin metal surfaces [21, 22], plasmon resonances and inter-coupling of metallic nanoparticles [23, 24, 25, 26], SPP propagation on gratings and waveguides [27, 28] are some of the examples to the SPP related studies that are part of nanophotonics.

These two examples on photonic crystals and SPP have a common denominator. They had to await the evolution of nanotechnology —manipulation of materials down to the atomic scale— from concept [29, 30] to a certain level of reality to fabricate accurate and advanced nanophotonic materials. Today, with a large number of nanofabrication techniques, a myriad type of materials are designed and engineered to study and understand optics at subwavelength scales. Electron beam lithography [31], focused ion beam (FIB) milling [32], photo electrochemical and reactive ion etching [33], self assembly [34], vapor liquid-solid (VLS) growth mechanism [35, 36], nanoimprint [37] can be counted as some of the techniques used for the benefit of nanophotonics. Furthermore, advanced nanocharacterization techniques; near-field microscopy with different type of nano-probes [38, 39, 40], angle-resolved cathodoluminescence microscopy [41], non-invasive optical imaging [42], dark-field microscopy [43, 43, 44], etc. in addition to developments in the computational techniques, simulation tools in the last fifteen years have made a remarkable impact on the understanding of light at the nanoscale.

The goal of this thesis is to come up with novel approaches on the fabrication of nanophotonic materials using a multi-functional nanofabrication machine, a so-called 'dual beam system' as it contains a focused electron and ion beam systems in the same instrument. Material removal and deposition are two of the main features of the system. Additionally, the machine has a scanning electron microscopy capability which enables us to see the result of the fabrication just after the processes.

Material removal with the dual beam system is established with either milling or etching processes. In the milling there is an interaction between a focused ion beam and a sample substrate. The momentum of the incoming ion is transferred to the substrate atoms in a sputtering process. A surface atom is ejected from the substrate provided that the transferred energy from the incoming ion is high enough to overcome the surface binding energy (SBE) [45]. A controlled movement of the focused ion beam allows the substrate to be shaped in an intended geometry. This milling technique even allows for the fabrication of 3D nanostructures. In the etching process a gaseous precursor is delivered to the system and absorbed by the substrate. Material removal as a gaseous by-product is generated upon a chemical reaction —between the substrate and precursor— which is assisted and enhanced by the focused ion or electron beam irradiation [46].

Material deposition can be established with either an ion beam or an electron beam. Similar to the etching, a gaseous chemical is delivered very close to the substrate surface and ion or electron beam assisted reaction converts the absorbed precursor molecule to an intended local solid deposition.

FIB based deposition is generally used for nanomachinery. Matsui and co-workers [47] presented examples of nanostructures built with FIB induced deposition such as parallel nanobeams and free-standing nanosprings.

In the electron beam induced deposition (EBID) the focused Ga^+ ion beam is replaced with focused electron beam. As, compared with FIB, the angular spread of secondary electrons is smaller. EBID allows the fabrication smaller nanostructure (down to 1 nm) arrays with higher accuracy [48, 49].

Fabrication of nanophotonic materials using FIB based deposition is not used mainly due to the Ga doping in the deposited material as most FIB system are still based on Ga^+ ions. The Ga^+ acts as a contaminant that is generally detrimental to the optical properties. Graells and co-workers [50] fabricated a monopole gold nanoantenna array with an organometallic precursor: *dimethylgold-acetylacetonate* (Me_2Au(acac)). However, EBID of metals with the organometallic precursors, like Me_2Au(acac), comes with high impurities and therefore requires post-production treatment such as annealing [51]. However, this annealing causes shape deformations of the deposited nanomaterials. A new method is therefore required to fabricate 3D plasmonic nanostructures with EBID.

1.2 Outline of this thesis

In this thesis we show that EBID can be used as a versatile nanofabrication technique to produce complex three-dimensional nanoplasmonic antennas. Additionally we also show that due to the local deposition capability EBID can also be exploited to tune the electromagnetic property of the nanostructures.

Chapter 2 is devoted to describing the basics of EBID. While it is a versatile and one-step nanofabrication technique, the process takes place as a result of complex interactions of various parameters. In this chapter we briefly explain the technique, describe the parameters and the interactions between them.

In **Chapter 3** we demonstrate the optical properties of ground plane monopole antennas. Core-shell type high aspect ratio nanoantennas are fabricated with EBID of silica and subsequent conformal gold coating. With angle-resolved CL measurements we investigate the dispersive plasmonic nature of the nanoantennas in the visible domain. Numerical calculations are used to deepen the understanding of the emission patterns of the antennas and calculate the effect of the core and shell thickness to the effective index, and therefore effective length, of the nanoantennas.

In **Chapter 4** we present the fabrication of a nanoantenna array composed of three-dimensional helical structures with EBID of silica and subsequent conformal gold coating. The effect of fabrication parameters on the yield and helix geometry is investigated. The mechanism behind the complex 3D helical nanostructuring is described in detail.

In **Chapter 5** we perform the optical characterization of the core-shell helical nanoantenna array. We demonstrate the optical activity of our structures by revealing the transmission dependency to the polarization state of light. To support and better understand the measured results we also perform finite element modeling based numerical calculations.

In **Chapter 6** we demonstrate how to exploit the local deposition capability of EBID of silica to load the gap of split-wire gold nanoantannas. Gap areas of the individual nanoantennas are filled with various amount of silica. Optical characterization of each structure with cathodoluminescence spectroscopy reveals red shifts on the resonances. It is observed that the amount of the red shift is directly related to the amount of silica deposition.

Chapter 2

Basics of EBID

The fundamentals of electron beam induced deposition (EBID), as a bottom-up, one step nanofabrication technique, are explained. The general working principles of EBID are described by separately considering the gas-solid, electron-solid and electron-gas interactions. After describing the apparatus used for EBID, the main principles of silica deposition with EBID, which is the core of this thesis, are described in further detail.

2.1 Introduction

Electron Beam Induced Deposition (EBID) is a versatile direct-write fabrication method which allows rapid fabrication of well-defined structures at nanometer scales without the need for a resist. The resistless nature makes EBID a more straightforward nanofabrication technique compared to other resist-based lithography techniques. For example the fabrication of plasmonic nanostructures with electron beam lithography requires several steps to obtain a 2D structure at the end [52]: spincoating a flat surface with a resist, electron beam exposure of the designed pattern, developing, coating the surface with metal and lift-off of the unwanted parts.

EBID's versatility is also due to the possibility of the deposition of a variety of materials; metals, semiconductors and insulators. Moreover, it has the ability to work not only on flat surfaces, but also on non-flat surfaces such as AFM tips, micro- or nanowires, *etc.* Beard and co-workers [53] fabricated cylindrical 'nanoneedle' structures on an atomic force microscope (AFM) probe tip which could be used for accurate imaging of surfaces with high and steep features. The diameter of the 'nanoneedles' varied from 18 to 100 nm. Hernandez and co-workers [54] realized electrical contacts between nanowires and microelectrodes with EBID. Another major advantage of EBID is the ability to fabricate 3D nanomaterials with very high aspect ratios and complex geometries [55].

During the deposition process a tightly focused (down to sub-10 nm) electron beam dissociates a gaseous precursor molecule by breaking the chemical bonds between the material to be deposited and the other chemical constituents of the precursor. The precursor is supplied in the vicinity of the substrate by a gas injection system (GIS). After the dissociation of the precursor, a solid material is deposited on the substrate and a volatile by-product is removed from the chamber by the vacuum pumps.

2.2 History

The exploration of electron beam assisted deposition goes back to the early days of electron microscopy. With the invention of the electron microscope [56], an intrinsic problem was quickly realized: following irradiance by the electron beam a carbonaceous contamination layer was typically formed on the substrate [57]. Hydrocarbons and water molecules combined to form this contamination layer when they decomposed on the substrate. The contamination was attributed to the interaction between the electron beam and adsorbed molecules on the substrate [58, 59]. These hydrocarbon and water molecules originated from poorly cleaned samples or from the vacuum system of the microscopes. It did not take too long to exploit this intrinsic problem of electron microscopy as a unique tool for nanostructuring. Baker and co-workers [60], in 1961, reported the first metallic thin film deposition by using an organometallic precursor dissociated with the electron beam. Similarly carbon film deposition was established by Hart and co-workers [61] with a carbon-containing gas precursor. A controlled carbon layer was deposited and a study of the gas pressure and substrate temperature on the deposition process was performed.

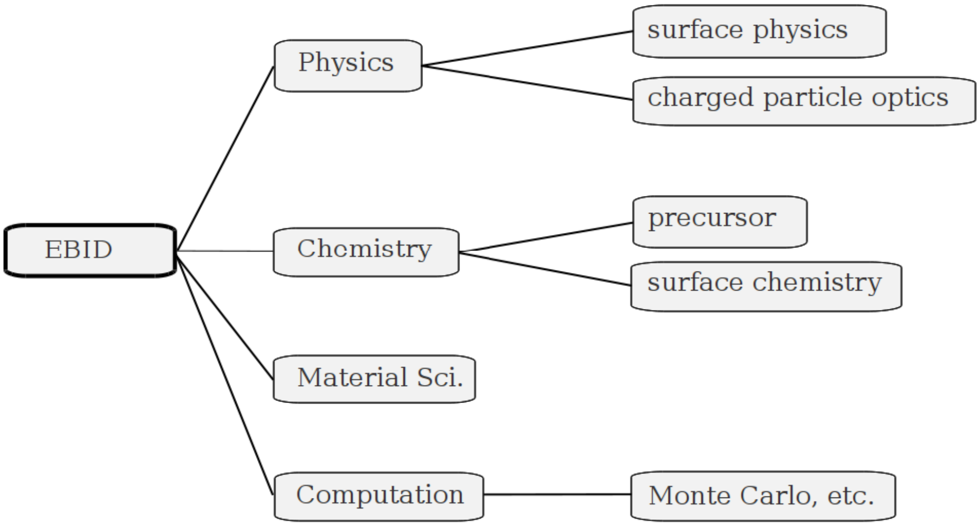

Figure 2.1: Complexity of the EBID process. Understanding and controlling the EBID process requires knowledge and expertise in a variety of fields

2.3 Fundamentals of EBID

2.3.1 Main principle

The main principle behind EBID is simple. A gaseous (precursor) molecule is delivered close to a substrate inside the vacuum chamber of an electron microscope. Scattered electrons from the substrate dissociate the precursor molecules to obtain an intended solid deposit and a gaseous by-product. However, actually exploiting this simple principle for the controlled growth of 3D structures at the nanoscale is far from simple and requires a combination of various expertise —from physics to chemistry, computational science [62] to material science— in order to understand and control the mechanisms involved [63, 64, 65] (see the diagram in figure 2.1).

In this chapter we give a brief outline of the main ingredients needed to perform EBID, followed by an overview of the three main processes: gas-solid, electron-solid and electron-gas interactions. It should be noted that detailed explanation of the interactions is beyond the scope of this thesis, as each process itself is extensive enough to be the topic of its own book.

2.3.2 Instrumental components

The essential instrumental components of EBID can be categorized as follows: a gaseous precursor that contains the molecules to be deposited, a focused electron beam and a gas injection system (GIS).

Precursor

A chemical compound (either gaseous, liquid or solid) which contains the material to be deposited following a reaction with the focused electron beam, is called a precursor. EBID allows various types of materials to be deposited, ranging from insulators to metals. Some of these are listed in table 2.1. The general properties of a precursor [66, 67] can be described as follows: being stable during storage and delivery for deposition, fast evaporation without residue inside the crucible, having a by-product after dissociation that is volatile at room temperature to allow removal from the chamber by pumping and decomposition to the desired solid material in a fast, clean and selective way.

Material	Precursor	Reference
Al	$Al(CH_3)_3$	[68]
Au	Me_2Au(tfac)	[69]
C	$C_{14}H_{10}$	[70]
GaAs	TMG and AsH_3	[71]
Si	SiH_2Cl_2	[72]
Si_3N_4	N_2 (Nitrogen on Si (100))	[73]
SiO_x	TEOS	[74]
TiO_x	$Ti(-OC_3H_7)_4$	[75]

Table 2.1: A list of often used materials that can be deposited with their respective precursors. For more information and a longer list see ref. [76]

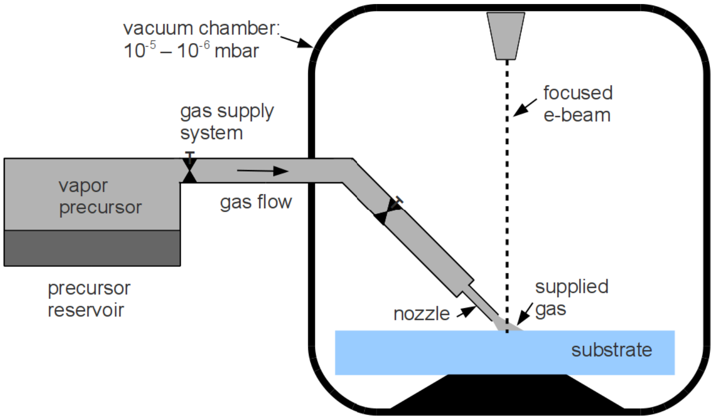

Figure 2.2: A schematic picture of a GIS that is used for EBID (adapted from ref. [77]). The precursor (solid, liquid or gas) is stored inside the reservoir. The gas flow is controlled by regulating valves in order to maintain the low pressures needed to keep the electron microscope operational. The nozzle is brought close (150±5 μm) to the substrate before EBID processing.

Electron beam

The energy of the focused electron beam is easily sufficient to break the bonds of precursor molecules adsorbed on a substrate. A scanning electron microscope (SEM), a transmission electron microscope [78] (TEM) or a scanning tunneling microscope [79] (STM) can be used to obtain a focused (or concentrated) electron beam. Among these microscopes a SEM is the most commonly used [80]. A typical SEM provides 1 kV to 30 kV acceleration energy for the electron beam. The current and focused beam size vary from 1 pA to 20 nA and from 2 to 100 nm, respectively [81]. Please note that the primary focused electron beam is responsible for only a negligible fraction of dissociation events during EBID (see below).

Gas injection system (GIS)

Whichever type of electron microscope is used for delivering the electrons, a GIS is required to supply gaseous precursor molecules onto the substrate surface. A GIS consists of the following parts [81]: a reservoir, a supply system and a nozzle

The precursor (solid, liquid or gaseous) is stored in a reservoir (see figure 2.2). The constant flow of the precursor gas through the nozzle is established by a gas supply system. The gas flow rate (throughput) Q and precursor molecule flux Φ at the substrate surface are the parameters that characterize a GIS for EBID processing. Q is expressed as molecules per unit time and Φ is expressed as molecules per unit area and unit time (molecules/cm$^2\cdot$ s). The flow rate in a GIS is typically controlled in one of three different ways [81]: with flow regulators, with a GIS flow conductance or with a heating system. The maximum flow rate is determined by the maximum operational pressure range of the electron microscopy system of typically 10^{-5} mbar [82]. Additionally for a GIS working with a heating system the temperature of the precursor must be kept low enough to prevent any chemical reaction which may alter the chemical composition of the precursor.

A typical GIS nozzle is typically 500 μm in diameter. Before the deposition operation the nozzle is inserted to a distance of 150 μm with a typical accuracy of 5 μm from the substrate surface [83]. After an operation period Δt the total throughput becomes $Q=(\Delta \mathrm{m}/\Delta \mathrm{t})\cdot(\mathrm{N}_A/\mathrm{M})$, where N_A is Avogadro's number, M is the molar mass of the precursor molecule

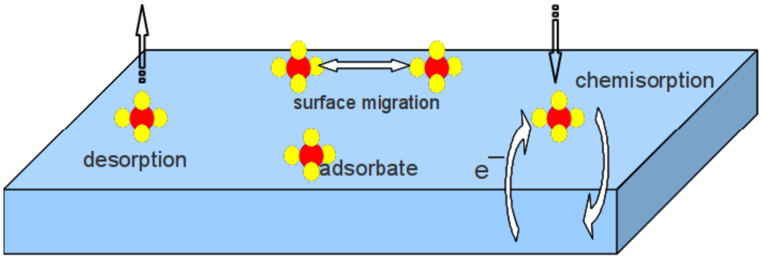

Figure 2.3: An illustration (adapted from [76]) showing the processes occurring when the precursor is adsorbed on a solid substrate.

and Δm is the total delivered mass of the precursor. The flux through the nozzle aperture then becomes,

$$\Phi = \frac{4Q}{\pi r_i^2}, \tag{2.3.2.1}$$

where r_i corresponds to the inner diameter of the nozzle.

2.3.3 Precursor-solid interactions

The precursor–solid interactions can occur under complex chemical and physical conditions. These interactions (figure 2.3) depend on a myriad of parameters: the chemical properties of the precursor and substrate, temperature, residence time (the time that a molecule is adsorbed on the surface), localized gas pressure and the angle of the GIS nozzle. The combination of all these parameters affects the yield of the deposition. Increasing the yield of the deposition depends on the optimization of the effective localized gas flux at the substrate surface area where the deposition takes place. It can be done in two ways: by increasing the gas throughput (Q) through the nozzle and by optimization of the effective coverage area of the precursor on the substrate surface. Increasing the gas throughput is limited by the choked flow [85] and the operational vacuum chamber pressure. Optimization of the effective projected area is established by aligning the nozzle in a way to obtain a short nozzle-substrate distance and low nozzle-substrate angle. Kohlmann and co-workers [84] developed a model (see the schematic illustration in fig. 2.4) to determine the effective gas coverage area A_a:

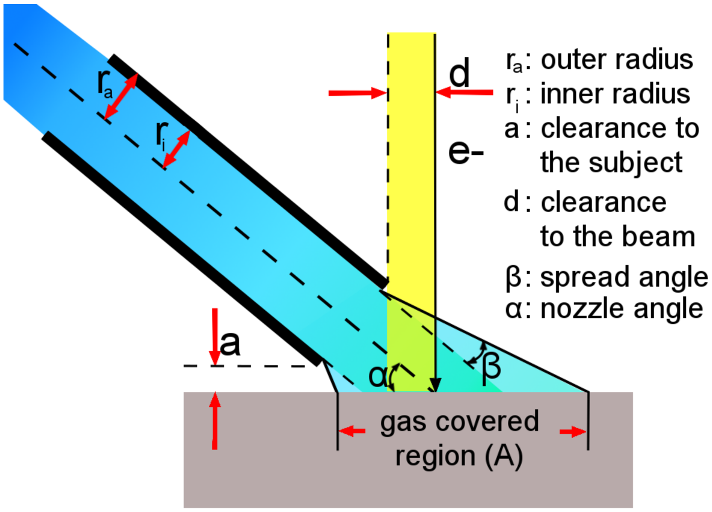

Figure 2.4: A schematic picture shows the parameters that affect the gas teh covered area of the precursor delivered by a GIS needle. (Adapted and modified from refs. [84, 76])

$$A = \pi\left(r_a cot(\alpha) + \frac{a}{\sin(\alpha)} + \frac{r_i}{\tan\beta}\right)^2 \sin^2(\beta \cdot C \cdot D), \qquad (2.3.3.1)$$

where

$$C = \frac{\sin(\alpha)\cos(\beta)}{\cos^2(\beta) - \cos^2(\alpha)},$$

and

$$D = \sqrt{C^2 + \left(\frac{\cos(\alpha)}{\cos(\beta) + \sin(\alpha)} + \frac{\sin(\beta)\cos(\alpha)}{\cos^2(\beta) - \cos^2(\alpha)}\right)}.$$

r_a and r_i are the outer and inner radii of the nozzle, respectively, a is the nozzle-substrate clearance, d is the clearance of the electron beam impinging on the substrate, β is the spread angle of the gas and α is the nozzle angle with respect to the substrate surface. By knowing the gas throughput (Q) from the nozzle and effective gas coverage area (A) on the substrate surface, the gas flux (Φ_{mol}) on the substrate surface can be calculated. And surface density (N_a) of the precursor molecules as a function of residence time (τ_a) of the molecule and gas flux is as follows:

$$N_a = \tau_a \Phi_{mol}, \tag{2.3.3.2}$$

where

$$\tau_a = \frac{1}{\upsilon} \exp\left(\frac{E_{des}}{kT}\right). \tag{2.3.3.3}$$

υ is the vibrational frequency of the precursor molecule, E_{des} is the desorption energy of the molecule, T is the temperature, and k is Boltzmann's constant. Equations 2.3.3.2 and 2.3.3.3 make it clear that the yield of the EBID depends on the local gas flux and the temperature. Higher local flux increases the probability of a reaction between the focused electron beam and the precursor molecule. Similarly, the longer the residence time, the larger the probability of the decomposition of the gas molecule by an electron.

2.3.4 Electron-substrate interaction

Electron–substrate interactions occur as a result of either elastic or inelastic scattering. In an elastic scattering the incoming (primary) electron (PE) approaches the positively charged nuclei of the substrate with an impact parameter that prevents it from being captured but leads to a deflection from its original trajectory. Such electrons escape the sample without (too much) loss of energy. In an inelastic scattering the PE interacts with the bound electrons of the sample. The repulsive interaction between the electrons can cause some of the bound electrons to be emitted into the vacuum. The electrons that leave the sample as a result of elastic and inelastic scattering are called backscattered electrons (BSE) and secondary (SE) electrons, respectively. The typical electron-specimen interaction (onion-like) volume and energy spectra of the scattered electrons are shown in figure 2.5a and 2.5b, respectively. BSE and SE are typically distinguished from each other with a boundary at 50 eV. Electrons with an energy more than 50 eV are considered to be BSE, while with a smaller energy they are taken to be SE.

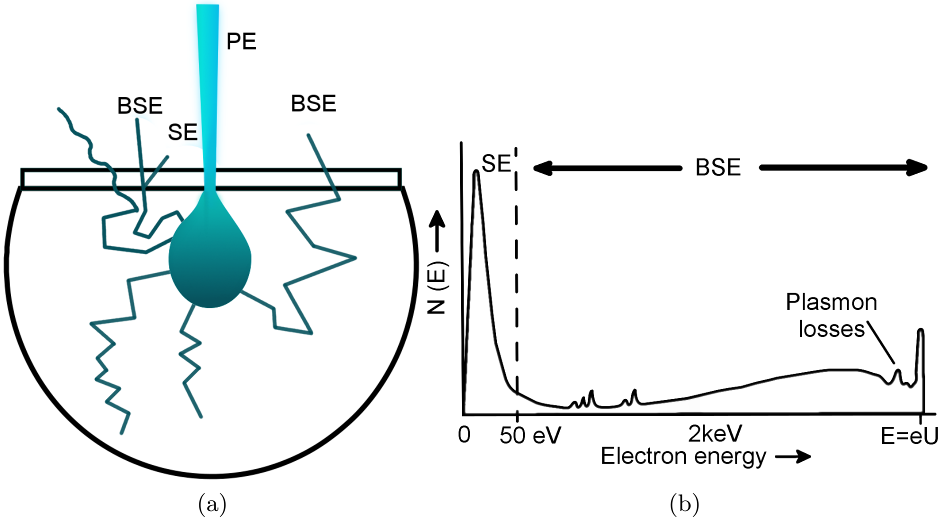

(a) (b)

Figure 2.5: (a) A schematic depiction of the consequences of a primary electron (PE) beam hitting a substrate, including the scattering (onion-like) volume of the incoming PE. BSE and SE stand for back scattering electrons and secondary electrons, respectively. (b) A characteristic energy spectrum of the scattering electrons in (a) as a function of their energies. The line of 50 eV marks a distinction between SE and BSE in terms of their energies. (Adapted from [86, 66])

2.3.5 Electron-precursor interaction

In principle the deposition process occurs when the adsorbed precursor molecules and scattered electrons interact on the surface of the substrate. The electron beam induced dissociation rate is given by the following formula [76]:

$$k = \sigma(E)\Phi_e \tag{2.3.5.1}$$

where σ(E) and Φ_e are the dissociation cross section as a function of electron beam energy and the electron flux (electron current per unit area), respectively. A broad area UV irradiation experiment [87] showed that deposition was dependent on the photoelectron emission yield of the substrate. Under the threshold of photoelectron emission there was no deposition. In other words the deposition took place due to the electrons emitted from the substrate.

Monte-Carlo simulations performed by Silvis-Cividjian and co-workers [88] showed that BSEs (with energy <1 keV) play an important role for the decomposition of the precursor molecules. The simulation results are also consistent with the experimentally observed lateral growth. However, in the work of Fowlkes and co-workers [89], an analysis of a tip growth behavior revealed that in addition to SEs and BSEs, the PEs also play a role in the deposition. The analysis based on Monte-Carlo simulation of the experiments of Fowlkes and co-workers indicated that while the vertical growth of the tip was caused by the PEs the lateral growth was caused by the BSEs and the SEs. Clearly, while there is no overall consensus it seems fair to say that both the primary and all kinds of scattered electrons contribute to different aspects of the electron beam induced deposition.

2.4 Silica deposition with EBID

In this thesis we use EBID of silica as a fabrication technique for the production of nanophotonic structures. Silica deposition can be performed with two different type of precursors [81]: (1) carbon-free precursors; silane (SiH_4) and silicon tetrachloride ($SiCl_4$), (2) organometallic precursors; alkoxysilanes Tetraethylorthosilicate (TEOS) and cyclic alky-siloxanes (TMCTS). TEOS is the preferred precursor for EBID processing due to the lower safety risk and ease of handling. At room temperature (20°C) TEOS is a colorless transparent liquid with a vapor pressure <1 mbar. The boiling point of TEOS is 121°C at 1 bar.

For our silica deposition water vapor is also used as a precursor gas in addition to TEOS. At room temperature the energy transfer from the electrons converts the precursor molecules to a solid silica deposition and vapor by-product according to following reaction:

$$Si(OC_2H_5)_4 + 2H_2O \rightarrow SiO_2 + 4C_2H_5OH, \qquad (2.4.0.2)$$

where C_2H_5OH (ethanol) is the volatile by-product that is removed by pumping. The liquid TEOS is stored inside the precursor reservoir and delivered by the GIS with a heating system. H_2O gas is stored in a special container (outside of the vacuum chamber) as a mixture with MgO crystalline particles. The H_2O reservoir is connected to the GIS inside the vacuum chamber via a pipe. During the deposition the TEOS and H_2O

valves open simultaneously and supply both types of molecules through the same nozzle.

2.5 Conclusion

In conclusion, we presented the fundamental principles of a versatile, bottom-up nanofabrication method, EBID. The instrumental components and their role in the deposition process are explained. It is shown that with various materials from insulators to metals can be deposited. Interaction amongst the substrate, electron beam and precursor molecules are briefly discussed.

Chapter 3

Dispersive ground plane core-shell type optical monopole antennas

We present the bottom-up fabrication of highly dispersive silica core, gold cladding ground plane optical nanoantennas. The structures are made by a combination of electron beam induced deposition of silica and sputtering of gold. The antenna lengths range are from 200-2100 nm with size aspect ratios as large as 20. The angular emission patterns of the nanoantennas are measured with angle-resolved cathodoluminescence spectroscopy and compared with finite-element methods. Good overall correspondence between the measured and calculated trend is observed. The dispersive nature of these plasmonic monopole antennas makes their radiation profile highly tunable.

3.1 Introduction

Antennas have been indispensable tool of modern human civilization ever since the first radio communication in 1898 [90]. They have been studied and engineered vigorously during the last 50 years in the radio frequency (RF) and microwave band of the electromagnetic spectrum. Research on their nanoscale optical counterparts has just been established in the last decade as parallel developments in nanotechnology [91, 92]. The purpose of all antennas (conventional and optical) is the same, either to localize propagating electromagnetic radiation or to convert localized energy to electromagnetic radiation. In other words the antenna is the translational structure between free-space and a guiding device in order to transmit electromagnetic energy from the transmitting source to antenna or from the antenna to receiver [93].

The combination of surface plasmon polaritons (SPP)—collective electron oscillations coupled to the external electromagnetic field—and nanoantennas makes it possible to squeeze the external electromagnetic field to dimensions much smaller than the diffraction limit. Reaching beyond the diffraction limit paves the way for novel single molecule microscopy [94, 95] and spectroscopy [96], near-field microscopy [97], surface-enhanced Raman spectroscopy [98], light harvesting for photovoltaics [99, 100] and light emission applications [101].

In this chapter we present a versatile and practical fabrication method for vertically oriented silica core-gold shell optical nanoantennas with aspect ratios as large as 20:1 (figure 3.1). To characterize the optical properties of these nanoantennas, we study their 3D emission pattern with angle-resolved cathodoluminescence (CL) microscopy [102, 103]. The results are compared with finite-element simulations that model the excitation of the nanoantennas by using a point-like dipole on top of each antenna. Additionally, effective index mode calculations were performed in order to elucidate the plasmonic properties of the nanoantennas and the role of the core and shell thickness.

3.2 Method

The silica core of the nanoantennas is fabricated by electron beam induced deposition (EBID) [104, 46]. Subsequently, a conformal gold shell is sputtered onto the silica pillars and the gold substrate. A Helios NanoLab 600 Dual Beam system equipped with a gas injection system (GIS) is used for the fabrication of the silica core.

The silica cores of the nanoantennas are grown on a substrate which is composed of a 30 nm gold layer coating a silicon wafer. The EBID of the silica cores proceeds as follows. Each nanoantenna core is composed of a series of disks with each disk deposited on top of each the last. The height of the nanoantenna is controlled by altering the number of disks deposited. Each disk is deposited by moving the focused electron beam around a series concentric circular tracks. The dwell time of the electron beam on each point of the track is 200 ns, and the total dose delivered (for the tallest structures) is 750 $nC/\mu m^2$. figure 3.1a shows an SEM micrograph of the fabricated structures, and figure 3.1b is a schematic representation of the nanoantenna design.

The measured height of the antennas is given in table 3.1: the tallest and shortest nanoantennas are 2100 nm and 200 nm, respectively. The average diameter (thickness), determined at half height of each antenna, is around 160 nm. A slight tapering is observed for each antenna of which the angle varies between 1.80° and 7°; the larger the antenna the smaller the tapering. After the gold deposition onto the silica pillars three of the longest antennas developed a bend which we attribute to the strain induced by the thermal contraction mismatch between Au and SiO_2 during cooling after the Au sputtering process.

Table 3.1: Height of the nanoantennas [nm]

rod no. 1	rod no. 2	rod no. 3	rod no. 4
2100±100	1550±100	1200±100	850±100
rod no. 5	rod no. 6	rod no. 7	
550±100	300±50	200±50	

3.3 Measurement with the angle-resolved cathodoluminescence

To study the optical properties of our nanoantennas we use CL microscopy. It is based on the coupling of a point dipole to the collective electron os-

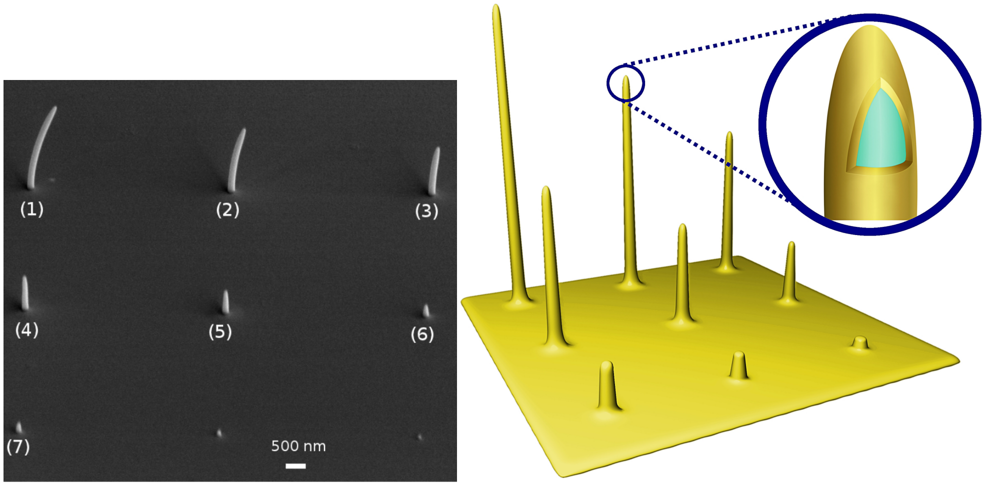

(a) (b)

Figure 3.1: (a) SEM image of vertically oriented core-shell nanoantennas grown on a substrate composed of a 30 nm gold layer coated on top of a silicon wafer. The SEM micrograph is taken at an angle of 52°. *The scale bar is 500 nm (b) A schematic representation of the nanoantennas. The silica core is fabricated by EBID on the substrate, after which 30 nm gold is deposited, covering both the antenna and substrate*

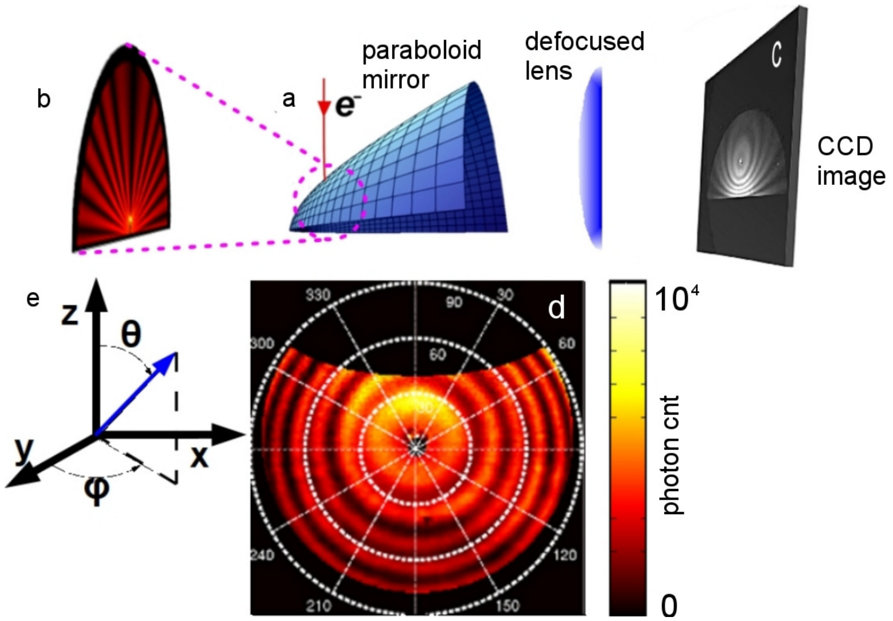

Figure 3.2: The angle-resolved CL setup: the sample at the focal point of the paraboloid mirror is irradiated by a focused electron beam of a SEM. The three-dimensional light emission is caused by the excited surface plasmons along the nanoantenna. The light is collected by a paraboloid mirror and sent to the CCD camera. The image with full wave vector information is converted to a polar graph where radial and angular coordinates correspond to azimuthal (ϕ:from 0° to 360°) and zenithal (θ: from 0° to 90°) spherical coordinates respectively.

cillations on the nanostructure. A point dipole is induced by the electrons from a focused beam of a scanning electron microscope (SEM), and the image charge of the incoming electron. The CL setup, incorporated into a FEI a XL-30 SFEG scanning electron microscope is composed of three parts: e-beam, a mirror and CDD camera. First, inside the vacuum chamber there is a paraboloid aluminum mirror with 0.5 mm focal length and a hole on the focal point through which the electron beam can irradiate the sample (see figure 3.2a). The light, emitted from the electron beam irradiated nanostructure (figure 3.2b) is collected by the paraboloid mirror and directed onto a CCD array (3.2c). The paraboloid mirror is designed

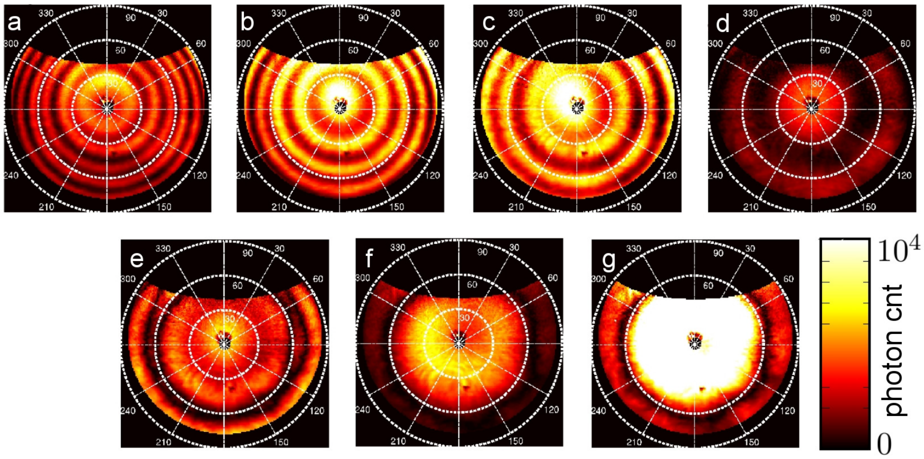

Figure 3.3: Measured angle-resolved emission patterns of nanoantennas at a wavelength of 650 nm. Each plot corresponds to the angle-resolved emission data of an individual antenna. From (a) to (g) the heights of the antennas are: 2100 nm, 1550 nm, 1100 nm, 800 nm, 550, 300 nm, 200 nm. respectively. The circular emission patterns correspond to the lobes that antennas radiate upon irradiation by electron beam. The color scale corresponds to the photon counts between 0 and 10000. In each measurement photons as are collected for 3 minutes. The lack of data on top of each graph between 50° *and* 310° *is caused by the parabolic mirror aperture.*

such that each pixel in the resulting image on the CCD array corresponds to a unique angle of emission from the structure. An optical filter is used to select only the wavelengths between 630 nm and 670 nm. Figure 3.2d shows the emission pattern of the longest nanoantenna.

Our angle-resolved measurement is performed by irradiation of the top of the each nanoantenna by the focused electron beam. The electric dipole excites the SPP mode(s) along the nanoantenna and with CL microscopy we observe the out-coupling of this mode(s) to the far-field. Figure 3.3 panels a - g show the angle-resolved emission data of the individual antennas tabulated in table 3.1 where the lengths of the nanoantennas vary from 2100 nm to 200 nm. This data is obtained by using a 650 nm bandpass filter with 40 nm bandwidth. The color scale in figure 3.3 shows the photon count collected from each of the seven nanoantennas. In figure 3.3a we see

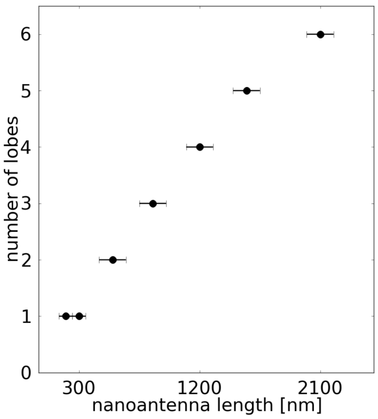

Figure 3.4: The measured relation between the length of the nanoantennas and the number of lobes of the emission pattern

that there are 6 circular patterns. We observe in figure 3.3a-g that the number of lobes decreases with the decreasing height of the nanoantennas. The measured linear relation between the number of emitted lobes and the nanoantenna height is plotted in figure 3.4

3.4 Simulation of antenna properties

3.4.1 Finite element modeling

The numerical calculations of our core-shell type nanoantennas are performed with COMSOL Multiphysics (4.2). COMSOL is based on solving partial differential equations (PDE)—especially Maxwell's equations in our case— with finite element method (FEM). In FEM the model structure is divided up into small mesh elements and solved by applying the relevant PDE on each mesh element. The mesh elements have a triangular geometry in our calculations. The type of the PDE is based on the problem to be solved *i.e.* for the electromagnetic problems the PDE are the Maxwell's equations.

Especially for 3D models the number of mesh elements is crucial to solve the problem within limited computational resources (memory and CPU power). Symmetry is an important geometrical feature to reduce the amount of mesh elements in the problem. Depending on the symmetry

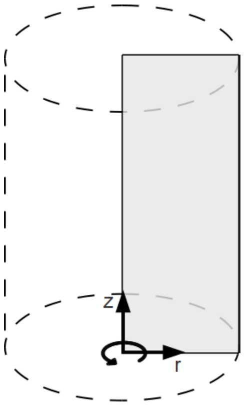

Figure 3.5: 3D cylindrical object by rotating a 2D geometry.

properties of the model structure, the number of elements can be reduced—by using appropriate symmetry planes—by factor of two or more. For example the 3D cylindrical geometry, central to this chapter, has a rotational symmetry. The whole 3D geometry can therefore be obtained by rotating the rectangular cross-sectional r-z plane around the axis (see figure 3.5), reducing the 3D problem to a 2D one.

3.4.2 Building the model for the ground plane nanoantenna

In our model we use the "2D axisymmetric" feature of COMSOL. This feature enables the calculations of 3D model structures that can be represented by 2D axially symmetric cross sections. For the calculations of our model structure we exploit the cylindrical geometry of the core-shell nanoantennas. The 2D cross-sectional geometry of the model is composed of half of a semicircle and rectangles for the cap and the main body of the nanoantenna, respectively (see figure 3.6a). The nanoantenna is positioned in the center of a calculation box shaped as half of a semicircle (see figure 3.6b). The base of the box corresponds to a gold substrate. The curved boundary of the calculation box is formed by a 750 nm thick perfectly matched layer (PML). The PML absorbs all energy incident upon it and eliminates reflections. The radius of the simulation box is 20 μm. The system is composed of three kind of material: gold, silica and vacuum. The shell of the nanoantenna and the substrate are gold. The core is silica and

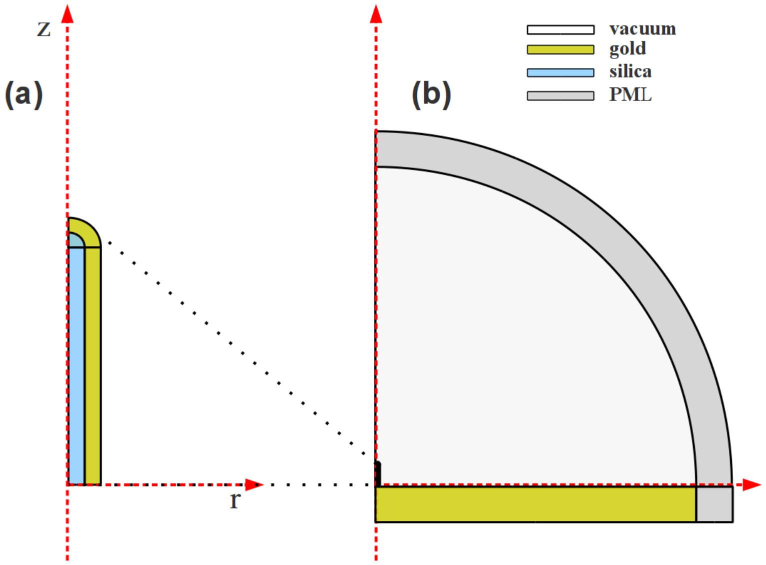

Figure 3.6: (a) 2D cross-sectional drawing of core-shell nanoantenna. (b) The nanoantenna is located inside a simulation box composed of a gold substrate and PML. The color code is used to identify the composition of the various parts of the model structure.

the whole system is in vacuum. For the gold the dielectric function from Palik [105] is used. For silica and vacuum the refractive indices 1.45 and 1 are used, respectively. In order to simulate the effect of the incoming electron beam, as an excitation source, a point dipole is positioned 1 nm above the top of the nanoantenna and oriented parallel to the z axis.

3.5 Comparison of the measurement with the calculation

In figure 3.7 the calculated 3D emission profiles of the all nanoantennas is shown. This 3D results are obtained by revolving the 2D (axially symmetric) solutions around the symmetry axis. The color scale represents the magnitude of the electric field around the nanoantennas. The emission profiles—going from figure 3.7*a* to (*g*)—belong to the nanoantennas listed in table 3.1 with the same sequence (from longer to shorter). In fig-

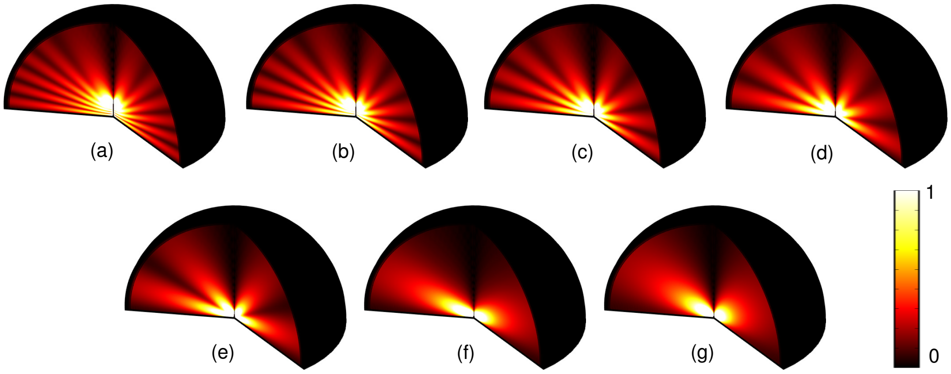

Figure 3.7: Finite element calculations of the magnitude of the electric field around the nanoantennas. The structure is inside the hemisphere simulation box. The walls of the hemisphere are totally absorbent (perfectly matched layer - PML) to eliminate interference due to the reflection from the walls. Antennas were excited by a point like electric dipole positioned on the top of the each rod. The dipole is oriented parallel to the nanoantennas' longitudinal axis. Color scale corresponds to the normalized E field amplitude.

ure 3.8 we compare the measured polar emission profile and the numerical calculations. In every polar plot the blue curves represent the measured photon count emitted by the nanoantennas at a 650 nm wavelength, while the red curves depict the numerical calculation of electric field intensity at the same wavelength. The measured and calculated values are independently normalized to their own maximum values. The experimental angular profiles are not precisely reproduced. This mismatch is attributed to the experimental uncertainties in the measured and estimated parameters of the nanoantennas. The measured parameters are the antenna height and core and gold thickness. In addition to those parameters the refractive index of the deposited silica core is not accurately known. The polar plot for measured data is obtained by cross-cutting the angle-resolved data along the radial axis. Both experiment and theory in figure 3.8 show the strong angular modulation of the emitted intensity. The number of lobes found in theory and experiment for the various length are in excellent agreement.

3.5.1 RF vs. nanoantenna in terms of the number of lobes

From a geometrical point of view our pillar-like nanoantennas, standing perpendicular to the gold surface, resemble ground plane antennas working in the RF regime. Standing perpendicular on top of a conducting plane has a role of creating a mirror image on the other side. Antennas working in the RF regime are assumed to be a perfect metal that reflects the electromagnetic field without penetration into the metal unlike their dispersive plasmonic counterparts [106, 107]. In order to illustrate the similarity and difference between the conventional ground plane (RF) antennas and our core-shell nanoantennas we perform a simulation of a RF antenna, *i.e.*, the dimensions of the nanoantennas and the measured wavelength are scaled up by 5 orders of magnitude in order to reach the low frequency RF regime. The ratio between the geometric antenna length and the wavelength (L/λ) is kept the same as that of nanoantennas. By keeping the geometric length to wavelength ratio the same we can get an idea of the effective length of the nanoantenna and RF antenna by counting the number of lobes in the emission pattern. The simulated RF antennas consist of a metallic ground plane, coaxial feed and a cylindrical antenna body. The entire system is inside a similar hemispherical simulation box as described above in section 3.4. The polar plot in figure 3.9 shows the comparison between the measurement on the longest nanoantenna and its simulated RF antenna

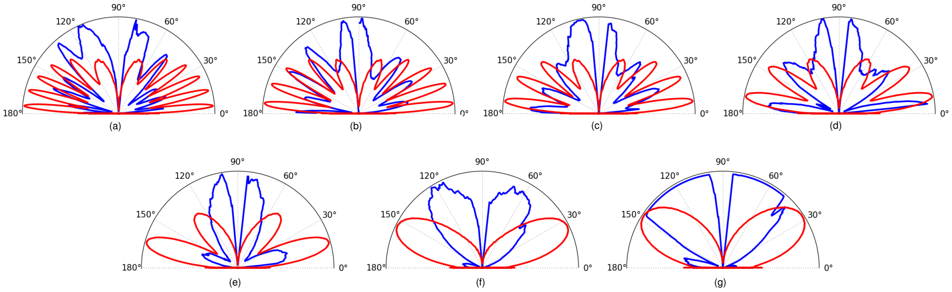

(a) (b) (c) (d) (e) (f) (g)

Figure 3.8: Comparison of the measured angle-resolved emission (blue line) and numerical calculations of the E field intensity (red line). Each data set are normalized with its highest data point i.e. maximum value on every polar plots corresponds to unity.

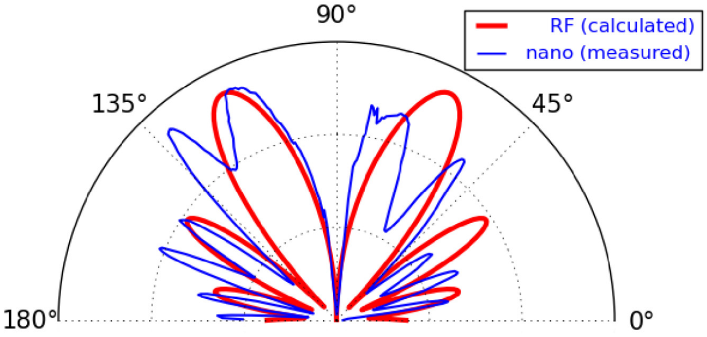

Figure 3.9: The number of emitted lobes of the longest nanoantenna is compared with its RF counterpart. The blue and red lines are associated with nano and RF antennas, respectively. The length of the antennas is 3.23λ where λ is equal to 650 nm and 6.5 cm for nano and RF antenna, respectively.

counterpart. The comparison is established in terms of the emitted number of lobes and the directivity. The blue curve corresponds to the measured photon emission rate of the longest (2100 nm) nanoantenna at 650 nm and the red curve corresponds to the electromagnetic emission at a wavelength of 6.5 cm of the 21 cm long RF antenna. Thus the antenna length is kept the same for both antennas (L=3.23λ). From the figure it is clear that the optical nanoantenna radiates 6 lobes (at the wavelength of 650 nm), whereas the RF antenna (at the wavelength of 6.5 cm) radiates 4 lobes. The effective length of our nanoantenna in the optical regime is therefore a factor of roughly 1.5 longer than its RF counterpart.

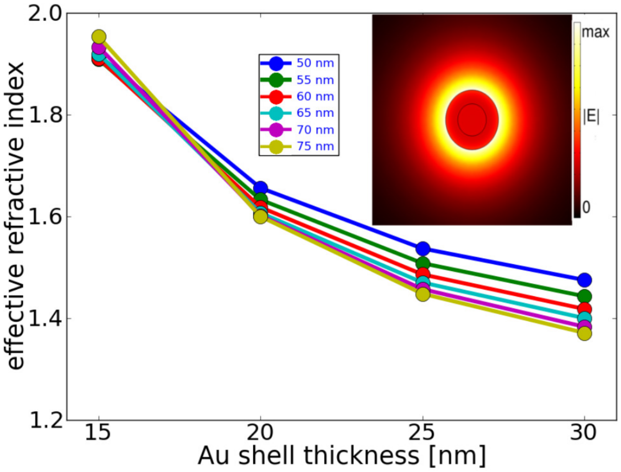

Figure 3.10: Calculated effective refractive index calculations for core-shell type nanoantennas as a function of gold shell thickness for different rod radius (from 50 nm to 75 nm).The E field intensity is shown as an inset for the antenna with 65 nm radius. n_{eff} is highly dispersive in terms of gold shell thickness and total rod radius.

3.6 Effective index calculation of the nanoantennas

After the comparison of the RF and nanoantennas we calculated the effective refractive index (n_{eff}) in order to clarify the role of the SPP on the nanoantenna's optical properties. COMSOL's mode solver feature is applied to an infinitely long nanorod composed of silica core and gold cladding. n_{eff} is calculated as a function of both Au shell thickness (which varies from 15 nm to 30 nm) and the radius of the silica core (50-75 nm) at 650 nm wavelength (see 3.10). The inset shows the radially symmetric mode [108] confined to the surface of the nanoantenna. The effective mode index,

$$n_{eff} = \frac{k_{SPP}}{k_0}, \tag{3.6.0.1}$$

determines by how much the effective length of a nanoantenna increases with respect to its geometrical length [109]. The result of the effective mode index simulation is depicted in figure 3.10. We observe that the effective refractive index of the core-shell nanoantenna depends strongly on both Au shell thickness and silica core radius. n_{eff} increases when either shell thickness or silica core radius are decreased. The maximum n_{eff} is observed for the thinnest Au shell (15 nm) combined with the smallest core radius (50 nm). The effective index calculation explains why the effective length of our nanoantenna is longer than that of an RF antenna. Indeed, for the 50 nm core radius antennas with a 30 nm thick gold shell effective refractive index is 1.47 (blue curve in 3.10), which is in excellent agreement with the ratio between the number of lobes found in our experiment and the simulation of an RF antenna. The plasmonic behavior and the dispersive refractive index thus strongly affect the radiation profile.

3.7 Conclusion

We have successfully fabricated high aspect ratio silica-gold nanoantennas by using electron-beam induced deposition (EBID) of silica combined with gold sputtering. The radiation profiles of the nanoantennas, with lengths in range 300-2100 nm, is measured using angle-resolved cathodoluminescence spectroscopy. The three-dimensional emission patterns and the numerical calculations reveal that the nanoantennas act as a ground plane monopole antennas with an effective mode index that is determined by silica core radius and gold cladding thickness. The large tunability of the antenna geometry with EBID in combination with the strongly dispersive plasmon propagation along the antennas enables the fabrication of optical antennas with tailored angular radiation profiles. [110, 111, 112]

Chapter 4

Fabrication of helical nanoantennas with electron beam induced deposition

In this chapter, we present a method for the fabrication of helical structures. The nanostructuring uses electron beam induced deposition (EBID) of silica and subsequent gold (thin) film deposition. The EBID parameters that directly affect the geometry and the yield of the fabrication are explained in detail. It is shown that even minor pressure differences of the precursors significantly affect the geometry of the structures. The mechanisms underlying the complex three-dimensional helical nanostructuring are also described.

4.1 Introduction

With the first experimental demonstrations of controlling and manipulating electromagnetic fields by using periodic structures composed of subwavelength building blocks [113] a new era is opened for light-matter interaction related investigations [114, 115]. The earlier studies in the visible spectrum of light were based on 2D structures however, for a number of applications and optical phenomena 3D structures are necessary [116]. To achieve the fabrication of 3D photonic structures various techniques, with various advantages and disadvantages, have been used. A particularly interesting class of 3D photonic materials are chiral nanostructures. Hoeflich and coworkers [117] fabricated 3D helical structures at the nanoscale with EBID of gold by using a dimethyl-gold(III)-acetylacetonate [Me_2Au(acac)] precursor. In this work it was shown that the annealing process after the deposition, to decrease the fraction of carbon in the helical structure, resulted in a significant shape deformation of the helical geometry.

Molecular self assembly [118, 119, 120] is a bottom-up nanofabrication technique based on DNA- peptide-directed assembly [121, 122] and is used for tailoring organic-metallic hybrid structures to fabricate nanoplasmonic materials [123]. By using a DNA origami controlled arrangement of gold nanoparticles, complex 3D nanoplasmonic structures can be realized. With this technique Kuzyk and co-workers [124] fabricated helical type plasmonic antennas that show optical activity in the visible wavelength range. They reported an accuracy of gold nanoparticle positioning better than 2 nm.

Direct laser writing (DLW) is another technique to fabricate complex 3D structures. With DLW Gansel and co-workers [125] fabricated a gold helix photonic metamaterial working at the far infrared regime. In DLW, a tightly focused femtosecond laser was controlled with piezoelectric actuators inside the volume of a polymer photoresist and two photon absorption phenomenon made it possible to build various type of 3D structures. The fabrication of the 3D polymer "mold" is followed by filling them with a metal (gold, silver, *etc.*) using electroplating. This has the advantage over EBID with Me_2Au(acac) of producing metallic structures with a high purity. The typical lateral resolution of DLW is 120 nm, [126, 127], a minimum lateral resolution approaching 65 nm can be reached with stimulated emission depletion DLW [128].

Electron beam lithography (EBL), exploiting the advantage of the sub-10 nm resolution of the electron beam, is widely used to fabricate 3D

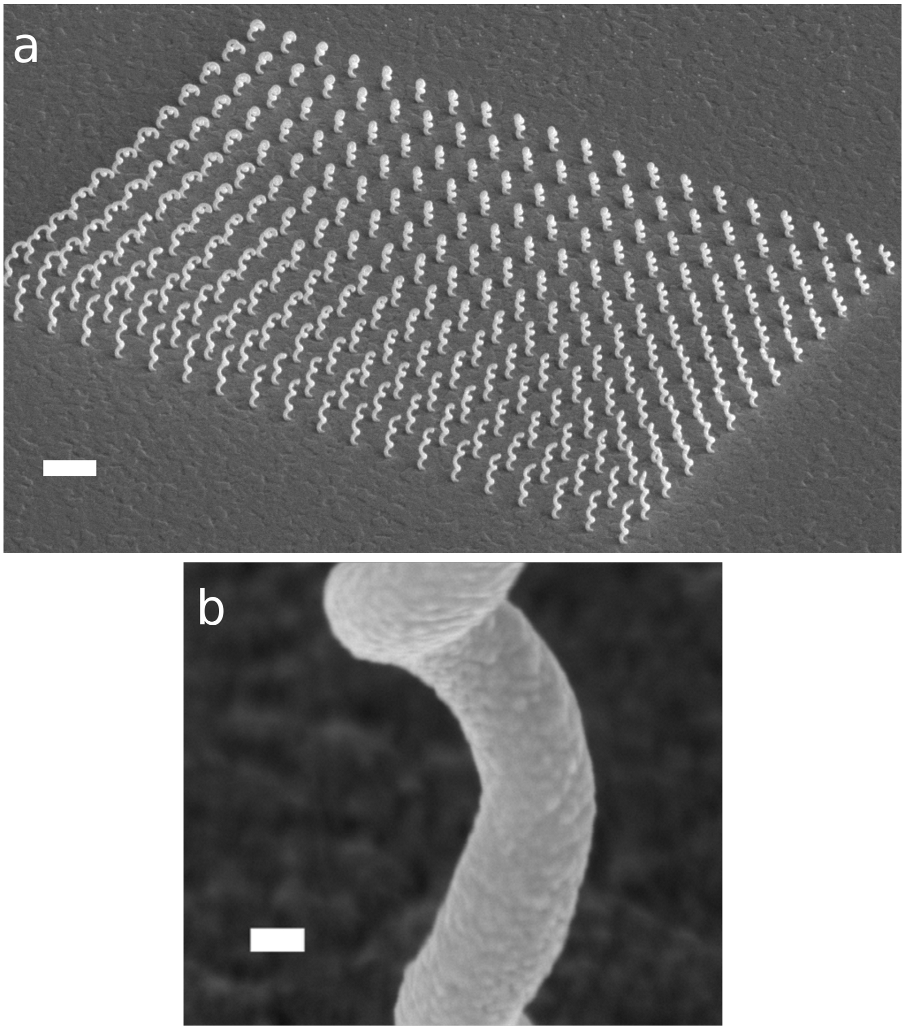

Figure 4.1: (a) SEM micrograph of an array of helical nanoantennas fabricated starting with EBID of silica. The substrate is glass coated with a 10 nm thin ITO film. After the deposition of the silica helix array the whole sample is conformally coated with a 30 nm thin gold film. The SEM micrograph shows the gold coated sample. The scale bar is 1 μm. (b) A close-up micrograph represents the surface roughness of a gold coated helical structure. The scale bar is 50 nm.

chiral plasmonic materials working at the visible spectrum. The "three-dimensionality" is achieved with stacked EBL based on a layer-by-layer fabrication. Each layer is aligned with respect to the previous one. So far, the most layers achieved with this technique is a five-layered photonic material [116]. Helgert and co-workers [129] produced an optically active chiral metamaterial working in the near-infrared regime. The material composed of two layers that each of them made up periodically arranged L-shaped gold nanoparticles. With the same technique, Hentschel and co-workers [130] fabricated plasmonic oligomers showing a strong chiral optical response in the visible domain. The fabrication of 3D complex nanostructures with the stacked EBL is a delicate and a time consuming process as it requires several steps of electron beam lithography (depending on the number of layers), lift-off and dry-etching processes.

In this chapter we describe the fabrication of a nanoplasmonic material composed of an array of helical antennas. We fabricate the helices with EBID of silica followed by a conformal coating of the whole sample with a 30 nm thin gold film. The combination of EBID of silica and gold sputtering results in a silica-core gold-shell helix array a micrograph of which is shown in figure 4.1*a*. A close-up micrograph in figure 4.1*b* represents the surface roughness of a gold coated helical structure.

Using the EBID of silica and gold thin film sputter deposition has several advantages to fabricate complex nanophotonic structures. Being a direct-write technique nanostructuring with EBID is established with a one step process. Using an electron beam with a sub-10 nm focus, like EBL, enables us to fabricate nanophotonic materials working in the visible regime. And deposition of silica followed by the deposition of pure Au saves us from a purification treatment [131] hence the shape deformation of the structures, after the deposition process [129]. In principle, any material that can be conformally deposited, can be used for the fabrication of the shell. Consequently we exploit the advantageous features of the direct write and electron beam lithography for building the array of helical nanoantennas.

4.2 Method

The helical structures are fabricated on a glass substrate coated with a 10 nm thick indium tin oxide (ITO) film. This conducting thin film prevents charging of the glass substrate due to the electrons used for the deposition.

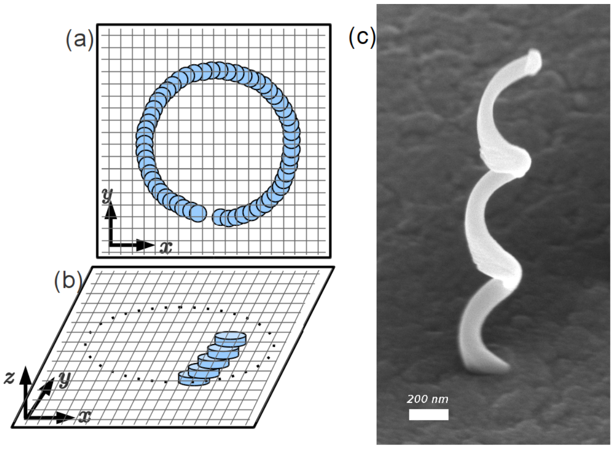

Figure 4.2: (a) Schematic representation showing the mechanism of helical nanostructuring. The structuring of an individual helix is established by moving the electron beam on a circular track with 0.5 nm step size. (b) In each step of the electron beam on its circular track there is a certain amount of deposition on top of the previously deposited material with an offset in the x and y direction along the circle. This offset is defined by the step size. (c) Tracing the electron beam three times along the circular path results in a three-pitch helical structure.

Such charging would deflect new electrons, that are used for EBID, thus preventing accurate fabrication of the nanostructures. ITO coated glass is used for the EBID fabrication because this substrate allows for a large range of optical transmission experiments to be performed. In practice to find the best combination of the beam current, energy and step size (explanations of those parameters is given in the section 4.2.2) requires a lot of trial and error.

4.2.1 Nanostructuring of the helix array

Having found the right combination of the EBID parameters, the next step is the structuring of the array composed of nanohelices. The x-y plane (field of view of the microscope) is divided into 2^{16} pixels. The actual size of each pixel depends on the magnification of the microscope's field of view. The higher the magnification the smaller the pixel size.

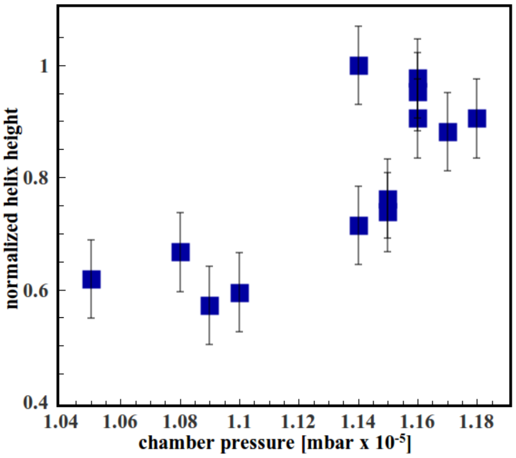

Figure 4.3: The correlation between the precursor pressure and the height of the helices. The plot shows the pressure of the vacuum chamber recorded at the start of the deposition process of each row. From the graph it can be seen that even a small fraction of pressure increase results in longer helices. The height of the helices are normalized to the longest one.

For our fabrication of an individual helix the electron beam is made to trace a circular path with a 0.5 nm step size which is defined as a sequential electron beam movement from pixel to another pixel. For this step size we use a 1.6×10^4 magnification which corresponds to a 0.25 nm pixel size. We choose a resolution with a pixel size two times smaller than the step size to have a smoother circular track. An even higher magnification than 1.6×10^4 would reduce the field of view thus limiting the overall size of the helix array that could be fabricated without the need for stitching. In each step of the electron beam a certain amount is deposited on top of the previously deposited material with an offset in the x and y direction given by the step size. Tracing the electron beam three times along the circular path results in a three-pitch helical structure (see figure 4.2).

4.2.2 The parameters and effects on deposition

Several parameters must be controlled, as they directly affect the 3D nanostructuring of the helical array. Namely: TEOS and H_2O pressure, the dwell time and step size of the electron beam and the electron beam current

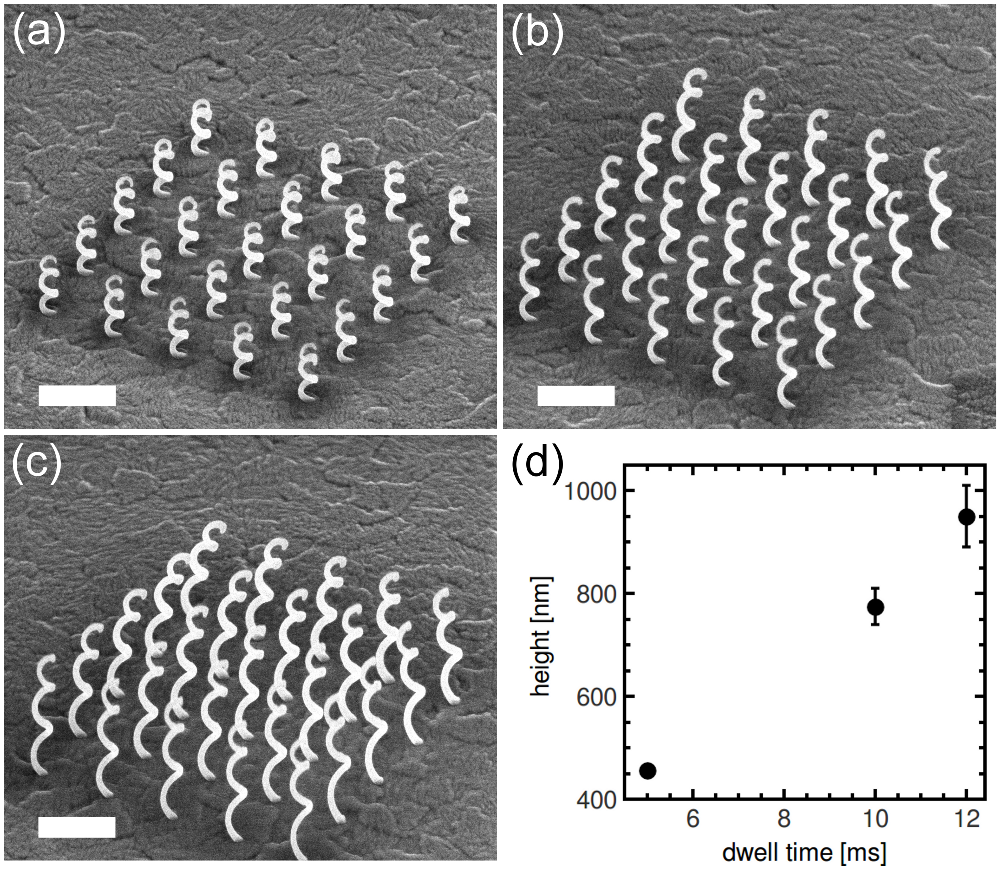

Figure 4.4: The effect of the dwell time on the height (pitch) of the helices. (a-c) SEM micrographs (with 500 nm scale bars) of helix arrays made with a dwell time of 5 ms, 10 ms and 12 ms, respectively. From these figures it can be seen that the pitch of the helices increases with increasing dwell time. The graph in (d) shows the helix height as a function of the dwell time.

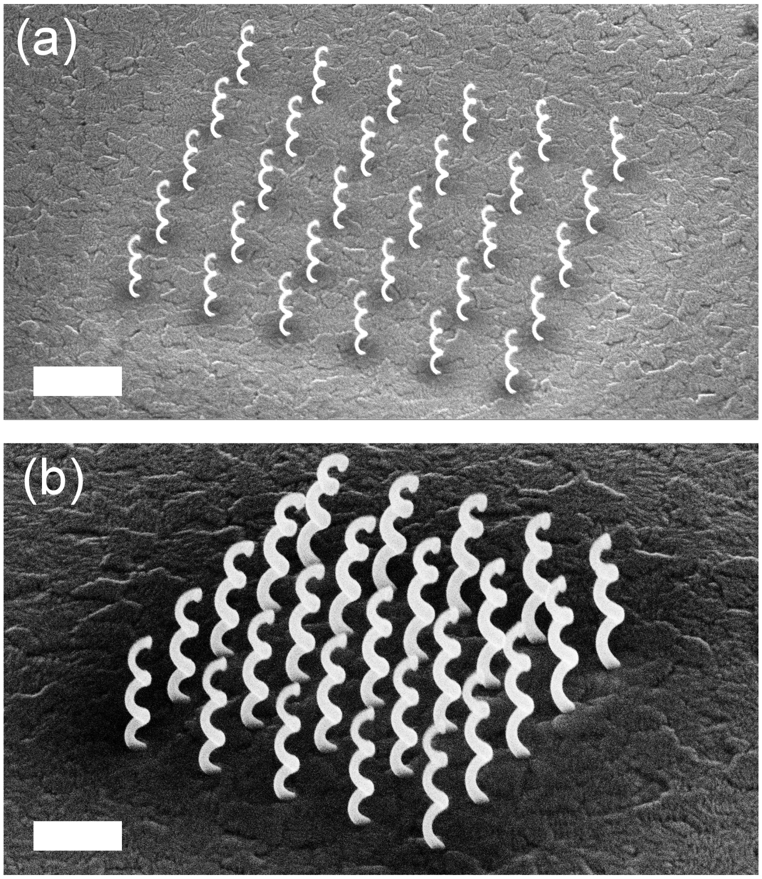

Figure 4.5: SEM micrographs of 5×5 helix arrays (a) and (b) fabricated with beam currents of 5 pA and 11 pA, respectively. The helix wires are thicker for the higher electron beam current. The acceleration energy for the structures shown in (a) and (b) is 3kV. The scale bars are 1μm.

Precursor pressure EBID is based on the conversion of a precursor gas(es) to a solid material on the substrate surface. The amount of precursor delivered directly affects the yield of the deposition, thus the geometry. In our case *tetraethoxysilane* (TEOS) and H_2O gases are used as precursors, delivered through the GIS. In the system that we use only the amount of water delivery can be manually controlled during the fabrication process which means that the pressure inside the vacuum chamber can be adjusted with the water valve only. According to our observations the TEOS partial pressure is more stable compared to the water pressure. During the helix array deposition the chamber pressure is kept at $1.12\pm0.05\times10^{-5}$ mbar which is dominated by the partial pressure of the H_2O.

We observe that the chamber pressure decreases during the deposition process. This indicates that the amount of precursor material delivered to the chamber decreases which results in less deposition and therefore shorter helices. To eliminate this effect we fabricate the helix array row by row with a pause between each subsequent deposition. Each row consist of 20 helices and takes roughly 180 seconds to complete. Despite the precautions, the row by row deposition strategy and adjusting the water partial pressure manually, in order to maintain a constant chamber pressure during the deposition process, there are unavoidable pressure variations. We observe that even small pressure variations can affect the overall result on the geometry of the helices. The plot in figure 4.3 shows the height of the helices as a function of the chamber pressure. Each pressure data point is taken just before depositing each row (the sequence of deposition is from left to right in figure 4.1). The corresponding helix height, normalized to the longest helix, is that of the last helix on each row (see figure 4.1). From the trend in this plot it can be seen that even a small fraction of pressure increase can cause height expansion of the helices; in this pressure regime a 10 % increase of pressure results in circa two times longer helices.

Dwell time The length of time that the electron beam stays at a point during its scan is called the dwell time. The amount of deposition on that point is related to the dwell time, *i.e.*, the longer the dwell time the more deposition. Higher dwell times result in longer helices due to the deposition of the wire along the vertical direction. The relation between the dwell time and the helix length can be seen in figure 4.4. The SEM micrographs in figure 4.4(a-c) show the deposited 5×5 helix arrays with three different dwell times: 5, 10 and 12 ms. The graph in the figure 4.4d shows the mean height of each helix array as a function of the dwell time. It can be seen from the graph that the height of the helices decreases with higher dwell time as a result of more material deposition caused by the longer dwell time of the electron beam on each deposition point. This observation reveals that by altering the dwell time we can tune the height (pitch) of the helices.

Electron beam current The electron beam current is the charge per unit time delivered by the electron beam. The dissociation rate is proportional to the number of electrons per unit time and has a direct effect on the deposition rate and the yield. In figure 4.5a and 4.5b we show two deposited 5×5 helix arrays with 5.4 and 11 pA beam current at 3kV acceleration energy. Based on the observation of the increasing pitch with increasing dwell time, a similar increase in pitch might have been expected for an increased beam current but the average height of the both helix array remains the same; 700±10 nm. However, increasing the current does result in thicker helix wires. The average thicknesses of the arrays shown in figure 4.5a and b are 35±4 and 65±4 nm, respectively.

The observations for the seemingly contradictory effect of the dwell time and the electron beam current suggest that these two parameters are effectively decoupled: increasing the electron dose by increasing the dwell time does not give the same result as increasing the dose by increasing the electron beam current. We explain this effect as follows: independent of the electron beam current, the number of adsorbed precursor molecules per unit area per unit time also influences the amount of deposition (see figure 4.2). Apparently the limited rate of arrival of new precursor molecules leads to a saturation effect. Increasing the current leads to a depletion in the center of the electron beam focus but enables more deposition in the flanks of the focus, leading to a wider helix. Increasing the dwell time actually allows more precursor molecules to be adsorbed during the deposition, leading to more vertical growth. It is very interesting and beneficial as two different aspects of the helical geometry can be tuned with those parameters independently.

4.3 Conclusions

In conclusion, we show that by using EBID of silica, in combination with gold sputtering, an array of complex three-dimensional metallic nanostructures can be successfully fabricated. The water pressure used for silica deposition turns out to be a critical parameter to the final outcome and should therefore be controlled carefully during the long fabrication process. We also show that the thickness of the helix wires can be controlled by the electron beam current and the height of the helices get longer with longer dwell time. The results presented in this work reveal that with the proper combinations of the EBID parameters; step size, dwell time and electron beam current, even more complex and more accurate three-dimensional nanostructures can be built provided that the pressure variation during the long time deposition process is improved.

Chapter 5

Optical activity of a chiral nanoantenna array

We investigate the optical properties of a nanoantenna array composed of core-shell type helical nanostructures. Optical transmission measurements with circularly polarized light reveal that the absorption of the nanostructures depends on the polarization state of the light. Numerical calculations are performed with finite element modeling on a single helical model structure. Good agreement between the absorption cross section based numerical calculations and measurements indicates that the helical nanoantenna array is an optical active material in the visible domain.

5.1 Introduction

Chirality is a very common phenomenon that can be observed at every scale of the universe from sub-atomic [132] to astronomical dimensions [133]. Since the nineteenth century chirality has played important roles in optics [134, 135], chemistry [136, 137] and elementary particle physics [132] to explore the basic foundations of the nature. A three-dimensional structure is defined as chiral if its plane mirror image cannot be superimposed on the original [138]. In other words a chiral structure has no symmetry elements of the second kind (a mirror plane, center of inversion, a rotation-reflection axis) [139]. The most well known chiral type object is a human hand. Whichever orientation is applied, the right and left hand cannot be superimposed. On a molecular level DNA—with its helical geometry—can be given as an example of a chiral structure [140].

The mirror image of a chiral object is called an enantiomer and except for its ‘handedness’ all scalar physical properties (molecular weight, electronic and vibrational frequencies, conductivity, elasticity, melting point, vapor pressure, etc.) are identical with its enantiomer [141]. A chiral object is distinguished from its enantiomer only in case of an interaction with another chiral entity. This feature makes the chirality one of the most interesting phenomenon especially in chemistry and biology [142]. As circularly polarized light has a chiral property, being either right or left handed, the optical response of the chiral molecules to the circularly polarized light is the fundamental tool of the stereochemistry that involves the study of the 3D arrangement of the atoms [143].

Chirality is also gaining significance in the context of metamaterials. A metamaterial is defined as an artificial structure with sub-wavelength building blocks (meta-atoms) [144, 145] causing unusual electromagnetic properties like negative refraction, super-lensing and cloaking. Control over the effective electric permittivity (ϵ) and magnetic permeability (μ) is one of the main driving forces of metamaterial research, including the simultaneous achievement of negative ϵ and μ. It was recently shown that with chiral meta atoms negative refraction can be obtained without negative ϵ and μ [146, 147]. The first experimental investigations on chiral matematerials were performed in microwave regime [148, 149] followed by the studies in optical domain [150, 129, 130]. Strong interaction of plasmonic ‘chiral-like’ (due to the in 2D planar geometry, they cannot be truly chiral) materials with circularly polarized light and also with chiral molecules [151] encourages the plasmonic based studies with real 3D chiral nanostructures. These 3D chiral nanoplasmonic materials can open new avenues for strong detection of chiral molecules [152], drug development and novel optical devices [125].

In this chapter we present the optical properties of a nanoantenna array composed of metallic chiral meta atoms. Transmission measurements with right and left hand circularly polarized light are performed to characterize the optical activity of our structure. Numerical calculations, to support and better understand the measured results, are performed with finite element modeling based commercial software.

5.2 Optical activity and circular dichroism

Some materials rotate the polarization plane of the light that propagates through them. These materials can be either solid or liquid. For the solids the rotation is a property of the crystal structure. For the liquid solutions the rotation occurs due to the geometry of the molecules, even when oriented in a random fashion. The ability of these materials to affect polarization comes from the chiral crystal structure of the solids and the chiral geometry of the molecules in the liquid. Crystalline quartz, of which the optical activity was discovered in the early 1800s [138], sodium chlorate, and certain kinds sugar are some examples of optically active materials [153, 154]. The rotation of the polarization is called optical activity and the materials that possess this feature are called optically active materials. The direction of the rotation depends on the type (handedness) of the chiral material. When the direction of rotation is to the right, observing from the side that the propagation of the light is towards the observer [155], the material is called right-handed (dextrorotatory), otherwise left-handed (levorotatory). The amount of the rotation per unit length inside the material is called rotatory power and depends on the wavelength. The wavelength dependence of the optical rotatory power is called rotatory dispersion [156].

The discovery of circular polarization (Fresnel, 1825) led to the insight that linearly polarized light (LP) can be regarded as a coherent superposition of right- (RCP) and left-handed circularly polarized light (LCP) with the same amplitude [157]. Hence, the rotation of the LP by optically active materials is ascribed to the relative phase differences of the circularly polarized light (CP). This phenomenon is explained in the following way:

suppose that a monochromatic linearly polarized light, with an angular frequency $\omega = 2\pi c/\lambda$—where c and λ are the speed and the wavelength of the light in vacuum, respectively—propagates along the z-direction inside an optically active medium. When at time t the electric field vectors of the RCP and LCP are parallel at $z = 0$ the direction of the RCP and LCP at position $z = d$ at time t would be, with respect to the directions at $z = 0$, $\theta_r = 2\pi cd/\lambda v_r$ and $\theta_l = -2\pi cd/\lambda v_l$, respectively. The phase velocities of the RCP(LCP) inside the medium are defined as $v_{r(l)}$. Hence, the rotation angle of the LP is written as [156],

$$\theta = \frac{1}{2}\left(\theta_r + \theta_l\right) = \left(n_r - n_l\right)\frac{\omega d}{2c} = \left(n_r - n_l\right)\frac{\pi d}{\lambda}, \tag{5.2.0.1}$$

where $n_{r(l)} = c/v_{r(l)}$ are polarization-dependent refractive indices of the medium. The specific rotation power is therefore

$$\rho = \frac{\pi}{\lambda}\left(n_r - n_l\right) \tag{5.2.0.2}$$

(For the derivation of the equations 5.2.0.1 and 5.2.0.2 see the Appendix 5.A)

The wavelength dependence of refractive index implies an absorption variation due to the polarization state of the light. The optical rotation and polarization dependent absorption are coupled to each other through a Kramers-Kronig relation [158],

$$\tilde{\rho} = \rho + i\psi, \tag{5.2.0.3}$$

where $\tilde{\rho}$, ρ, and ψ represent the complex rotatory power, rotation angle, and ellipticity that LP acquires upon propagation through the medium. This conversion from LP to elliptically polarized light is described by the decomposition of the linearly polarized light into the coherent RCP and LCP components with different amplitudes. The amplitude difference stems from the absorption difference of the medium with respect to the two types of CP. The ellipticity—in general the ratio of the major and minor axis of an ellipse—of a medium (ψ) is obtained from the ratio of the amplitudes of the RCP and LCP and can be formulated as

$$\psi \approx \frac{\pi}{\lambda}\left(\kappa_r - \kappa_l\right), \tag{5.2.0.4}$$

(see Appendix 5.B for the derivation of the equation 5.2.0.4) where $\kappa_{r(l)}$ corresponds to imaginary part of the refractive index for the RCP(LCP). Inserting the equation 5.2.0.2 and 5.2.0.4 into the equation 5.2.0.3 gives

$$\tilde{\rho} = \frac{\omega}{2c}\left[(n_r - n_l) + i\,(\kappa_r - \kappa_l)\right]. \tag{5.2.0.5}$$

The polarization-dependent absorption of the optically active medium, $\Delta\kappa = (\kappa_r - \kappa_l)$, is called circular dichroism.

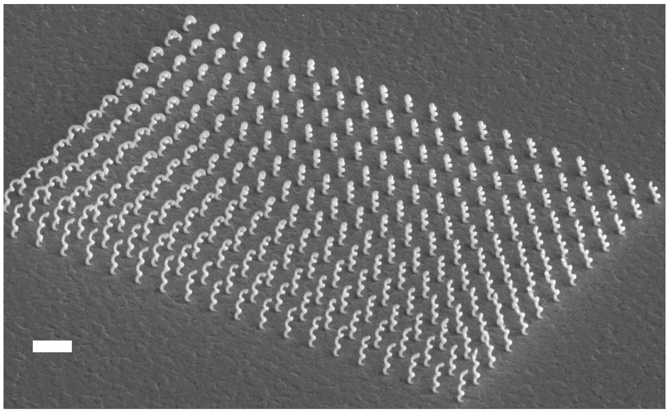

Figure 5.1: The nanoantenna array is composed of helix type chiral nanostructures. The sample is fabricated with EBID of silica and subsequent gold deposition (see Chapter 4). The scale bar is 1 μm.

5.3 Results and discussion

The sample (see figure 5.1) consists of an array of three-turn helical (right-handed) type core-shell chiral nanoantennas. The cores of the helices are silica fabricated with EBID and 30 nm shell is obtained by subsequent conformal gold coating. The nanoantenna array is composed of 20×13 helices. The distances between the adjacent helices in the horizontal and vertical directions are 750 nm. The main components of the optical setup for the measurements are shown schematically in figure 5.2. We use a super continuum laser as a light source. The light from the laser is circularly polarized with the combination of a linear polarizer and a quarter-wave ($\lambda/4$) plate. The sample is illuminated from the glass side. The transmitted

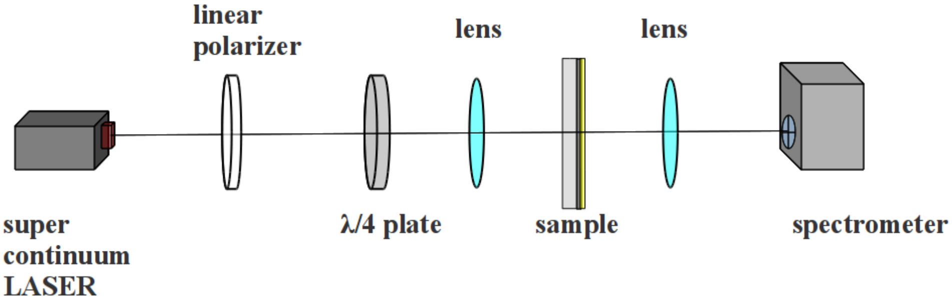

Figure 5.2: A schematic picture represents the main parts of the setup used for transmission measurements. The light coming from a super continuum laser is converted to circularly polarized light with a $\lambda/4$ plate. The transmitted light through the sample is collected with a grating spectrometer.

light is collected with a grating spectrometer. The focal spot size of the light is approximately 40 μm.

5.3.1 Experimental results

We measure the transmission of the array for RCP and LCP. The experimental results are presented in figure 5.3a. Red and blue curves represent the normalized transmission spectra of our nanoantenna array measured with the RCP and LCP, respectively. For the normalization, we use reference transmission measurements for RCP and LCP, separately, through an area of the sample without helices. For both polarizations a minimum in transmission is found at roughly 700 nm, which indicates a resonance in our structure. We attribute minimum in transmission to a plasmonic resonance. The position of this resonance will, to first order, be determined by the geometrical length of the antenna and the effective refractive index of the excited mode (see Chapter 3). The geometrical length of the antenna is hard to determine. Also given the sensitivity of the effective index on the antenna parameters (see Chapter 3), we cannot determine the number of nodes associated with the resonance.

The transmission difference between the RCP and LCP stems from the interaction of the CP with our chiral nanoantanna array in the following way: the light couples to the helical nanoantennas and forces the conduction electrons to move from their equilibrium positions. This displacement takes place as a helical current on each nanonantenna and causes electric and magnetic dipole moments parallel to the axis of the helices. The strength of the electric and magnetic dipole moments depend on the handedness of the circularly polarized light hence, RCP absorption is measured higher than LCP. In other words the transmission of the RCP through the helix array is lower than the LCP. The graph in figure 5.3b shows the relative transmission (RT) between the two polarizations. The RT curve is obtained from the ratio of the transmittances of the RCP with LCP. Figure 5.3b shows that the array exhibits circular dichroism. The details of this RT curve will be discussed in the next section together with a comparison with calculations.

5.3.2 Numerical calculations and comparison with the measurements

The numerical calculations are performed with the RF package of COMSOL Multiphysics (version 4.2). The software is based on solving the Maxwell's (differential) equations—of a given problem—with the finite element modeling. For our problem we design a spherical calculation box formed with air. A 900 nm thick outer shell of the calculation box is designed as a perfectly matched layer (PML) to eliminate reflections during the calculation process. A core-shell type helix is positioned at the center of the calculation box (see figure 5.4). The core and shell of the helix are composed of silica and gold, respectively. Palik [105] data is used for the optical parameters of silica and gold. The helix is excited with the RCP and LCP, subsequently. The wavevector of the exciting CP is parallel to the z-axis. Calculated results are analyzed in terms of the absorption cross section (ACS). The reason is two-fold. First, the calculated absorption is directly related to the transmission if scattering and reflection is ignored. Second, while the radius of the calculation domain for a typical transmission simulation problem should be at least a factor of twenty times the wavelength of incoming light, the radius of the calculation domain can be as small as the wavelength of the light for the ACS based simulations. This is a remarkable advantage from the calculation time and computational sources perspective. The ACS is obtained from the integration of time-averaged resistive heating of the helical structure. According to the Poynting theorem resistive heat is

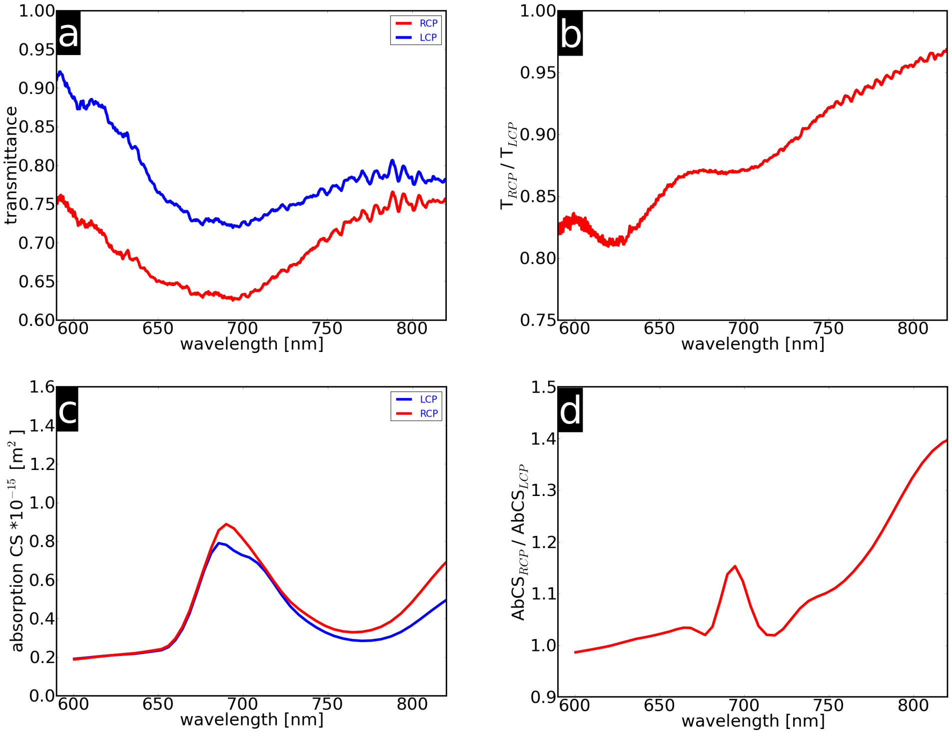

Figure 5.3: (a) Transmission measurement of the helix array with RCP and LCP are represented with the red and blue plots, respectively. (b) the optical activity of the helical array is represented with the relative transmission of the RCP with respect to the LCP (c) calculated absorption cross section of the helical model structure in terms of the RCP and LCP (d) the calculated optical activity of the helix model structure is represented with the relative absorption cross section of the RCP with respect to the LCP.

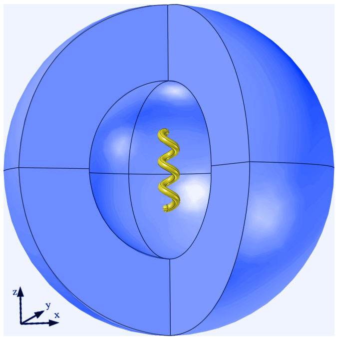

Figure 5.4: The model structure is positioned inside an air spherical calculation box composed of two parts. The 900 nm thick outer part, has a shell geometry, is designed as a perfectly matched layer (PML). In the inner spherical part the helical model structure is excited with the RCP and LCP, subsequently to investigate the optical activity of the structure.

described as

$$P_{rh} = \int_V (\mathbf{J} \cdot \mathbf{E}) dV, \tag{5.3.2.1}$$

where **E** and **J** represent the induced electric field and current density on the structure, respectively and V corresponds to the volume of the helix. The result is normalized with the impedance of the free space [159].

Figure 5.3c shows the calculated ACS of the helix model structure for RCP and LCP. As the absorption is calculated the resonances peaks should be compared to transmission minimums. The red and blue curves represent the ACS for the RCP and LCP, respectively. In figure 5.3c it is seen that the model structure is resonant at 700 nm. In addition, the absorption of the RCP is found to be higher than the LCP which is consistent with the measured transmission results (figure 5.3a)—where the transmittance of the RCP is lower with respect to the LCP. In figure 5.3d the calculated relative absorption cross section (RA) between the RCP and LCP is shown. The RA is obtained by dividing the absorption cross section of the RCP with the LCP. The peak at the resonance position stems from the absorption dependence of the helical model structure to the circular polarization state of the light. For our model structure the absorption of the RCP is 12% higher compared to the LCP.

Having compared the measured RT and calculated RA—both represent the optical activity of the helix array and helical model structure, respectively—it is seen that the RA has a sharper resonance feature than the RT. We attribute the broadening of the peak to inhomogeneity in the array: during the fabrication (EBID process) of the helix array typical parameter fluctuations can cause small deviations from the intended size and geometry of the helical structures. In the SEM micrograph of the helix array (figure 5.1) it can be seen that the helices on the left part of the array are longer with respect to the right part of the array. Similar size deviation is also seen between the upper and lower part of the array. While a comparison of the transmission measurement and ACS calculations revealed a plasmonic resonance at the same time wavelength with the same sign for the circular dichroism, differences are also apparent. In the calculations wavelength to the blue of the resonance exhibit almost no circular dichroism while the measurements do show circular dichroism that even seems to increase for shorter wavelengths. On the red side of the resonance exactly the opposite is observed although some circular dichroism is observed in the measurement. At present the cause of the difference is unclear. We suggest that as the calculations are based on the absorption only, the lack of scattering and reflection calculations may be (part of) an explanation for the difference. Furthermore the calculations are performed on a helical model structure without a substrate whereas a substrate is present in the experiment. This difference might be another factor for the difference between the trends on the measured transmission spectra and calculated ACS.

5.4 Conclusion

We present the optical properties of the nanoantenna array composed of chiral antennas. With transmission measurements we demonstrate that our helical nanoantenna array is an optically active material in the visible domain. Numerical calculations also indicates the optical activity at the same wavelength range of the measurements. This result demonstrates that with electron beam induced deposition complex three dimensional nanoplasmonic structures with novel optical properties can also be fabricated successfully. This breakthrough can open new avenues for numerous applications: for example designing chiral metamaterials without negative permittivity and permeability [147, 160] to achieve superlensing [161, 162, 163] perfect absorbing [164], cloaking [165, 166]. Sensing of optically active molecules on small areas and in small volumes [167], such as on thin films and in microfluidic devices.

5.A Appendix: derivation of the optical rotation equation 5.2.0.1

For the derivation of the optical rotation we use the Jones vector notation [168] where the RCP and LCP (propagating in the z-direction), respectively, are represented as follows [156];

$$\begin{bmatrix} 1 \\ -i \end{bmatrix} e^{i(k_r z-\omega t)} \quad and \quad \begin{bmatrix} 1 \\ i \end{bmatrix} e^{i(k_l z-\omega t)}, \tag{5.A.0.2}$$

where $k_{r(l)} = n_{r(l)}\omega/c$ correspond to wavenumber for the RCP(LCP).

With the Jones vector notation, after traveling a distance d inside an optically active medium a LP can be written in terms of RCP and LCP components as follows:

$$\begin{bmatrix} 1 \\ 0 \end{bmatrix} e^{i(kz-\omega t)} = \frac{1}{2}\begin{bmatrix} 1 \\ -i \end{bmatrix} e^{i(k_r z-\omega t)} + \frac{1}{2}\begin{bmatrix} 1 \\ i \end{bmatrix} e^{i(k_l z-\omega t)}, \tag{5.A.0.3}$$

where k is the wavevector in vacuum and the complex amplitude of the light after propagating a distance d inside the medium becomes;

$$\begin{aligned} &\frac{1}{2}\begin{bmatrix} 1 \\ -i \end{bmatrix} e^{ik_r d} + \frac{1}{2}\begin{bmatrix} 1 \\ i \end{bmatrix} e^{ik_l d} \\ &= \frac{1}{2} e^{i(k_r+k_l)d/2} \left\{ \begin{bmatrix} 1 \\ -i \end{bmatrix} e^{i(k_r-k_l)d/2} + \begin{bmatrix} 1 \\ i \end{bmatrix} e^{-i(k_r-k_l)d/2} \right\}. \end{aligned} \tag{5.A.0.4}$$

Inserting the expressions of ϕ and θ,

$$\phi = \frac{1}{2}(k_r + k_l)d \tag{5.A.0.5}$$

and

$$\theta = \frac{1}{2}(k_r - k_l)d, \tag{5.A.0.6}$$

turns the complex amplitudes into:

$$e^{i\phi}\left\{\tfrac{1}{2}\begin{bmatrix}1\\-i\end{bmatrix}e^{i\theta}+\tfrac{1}{2}\begin{bmatrix}1\\i\end{bmatrix}e^{-i\theta}\right\}=$$

$$e^{i\phi}\begin{bmatrix}\frac{1}{2}(e^{i\theta}+e^{-i\theta})\\ \frac{1}{2}(e^{i\theta}-e^{-i\theta})\end{bmatrix}=$$

$$e^{i\phi}\begin{bmatrix}cos\theta\\ sin\theta\end{bmatrix}, \tag{5.A.0.7}$$

where the equation 5.A.0.7 represents the rotation of the linearly polarized light inside the optically active medium. The θ represents the amount of the rotation. From the equation 5.A.0.6 and from the definition of the wavenumber in terms of refractive index; $k_{r(l)} = n_{r(l)}\omega/c$, where $n_{r(l)}$ is the refractive index of the RCP(LCP), we obtain,

$$\theta = (n_r - n_l)\frac{\omega l}{2c} = (n_r - n_l)\frac{\pi l}{\lambda}, \tag{5.A.0.8}$$

and the specific rotatory power per unit length is written as,

$$\rho = (n_r - n_l)\frac{\pi}{\lambda}. \tag{5.A.0.9}$$

5.B Appendix: derivation of the equation 5.2.0.4

The ellipticity of the light in terms of the amplitude differences between the RCP and LCP upon propagating through an optically active medium is described as follows [154];

$$tan\psi = \frac{E_r - E_l}{E_r + E_l}, \tag{5.B.0.10}$$

where $E_{r(l)}$ corresponds to the amplitude of the RCP(LCP). If $E_r > E_l$, ψ is defined to be positive and the rotation is clockwise. As the absorption is related to the imaginary part of the refractive index the attenuation of the light propagated a distance d inside the medium is represented as;

$$E_d = E_0 e^{-2\pi\kappa d/\lambda}, \tag{5.B.0.11}$$

where E_0 and E_d, are the amplitude of the light before and after propagating a distance d, respectively. κ, and λ correspond to the absorption index and free space wavelength, respectively. Substituting the equation 5.B.0.11 into the equation 5.B.0.10 we obtain,

$$\begin{aligned} tan\psi &= \frac{e^{-2\pi\kappa_r d\lambda} - e^{-2\pi\kappa_l d/\lambda}}{e^{-2\pi\kappa_r d/\lambda} + e^{-2\pi\kappa_l d/\lambda}} = \frac{e^{\pi d(\kappa_l - \kappa_r)/\lambda} - e^{\pi d(\kappa_l - \kappa_r)/\lambda}}{e^{\pi d(\kappa_l - \kappa_r)/\lambda} + e^{\pi d(\kappa_l - \kappa_r)/\lambda}} \\ &= tanh\left[\tfrac{\pi d}{\lambda}(\kappa_l - \kappa_r)\right], \end{aligned} \tag{5.B.0.12}$$

and for small ellipticity with a unit of radians per unit length the equation 5.B.0.12 can be approximated as follows;

$$\psi \approx \frac{\pi}{\lambda}(\kappa_l - \kappa_r), \tag{5.B.0.13}$$

which represents the circular dichroism explained in terms of the ellipticity.

Chapter 6

Loaded plasmonic split-wire nanoantennas

With the local deposition feature of the electron beam induced deposition (EBID) we load plasmonic split-wire nanoantennas. We deposit silica in the gap region of the gold nanoantennas. We measure the response of the split-wire nanoantennas with cathodoluminescence (CL) spectroscopy. As a result of the loading the resonances of the nanoantennas shift towards the longer wavelengths. As the amount of the deposited silica increases, so does the shift. The results are described with a heuristic model.

6.1 Introduction

Over the last decade as a consequence of advances in nanofabrication techniques, a depth of understanding and level of experience has emerged regarding the control of optical fields by means of the engineered plasmonic nanostructures [1, 169, 170, 171]. For example, nano-sized Yagi-Uda antennas—with similar elements as their conventional counterparts—can control the direction of the emission and the polarization state of light emitted by a quantum dot [96]. It was also shown that nanoantennas designed with the guidance of the classical circuit theory can behave as 'lumped' nanocircuit elements and exploited to control the light in the mid-infrared regime [172]. Theoretically it was suggested [173] that the optical response of a split-wire nanoantenna can be tuned with a nanoload positioned in the gap. The calculations revealed that the type, amount and combination of the loading materials used for filling the gap of the split-wire nanoantennas significantly affect the optical response [174, 112]. In these studies it was also shown that nano-loading the gap of these nanoplasmonic structures with semiconductor materials enables the active control of nanoantennas' optical properties by exploiting the nonlinear properties of the loading materials [175, 176, 177, 178].

In this Chapter, we show that local deposition with EBID can be exploited to tune plasmonic nanostructures. The 'tunability' of the split-wire nanoantennas is obtained by progressive silica deposition in the gap region of the individual split-wire nanoantennas. Cathodoluminescence (CL) spectroscopy is used to measure the change of the optical properties of the individual split-wire nanoantennas as a function of the amount of deposited silica.

6.2 Method

The split-wire nanoantennas used in this investigation are fabricated with electron beam lithography. The substrate on which the antennas are fabricated is composed of two layers. The upper part of the substrate is a 100 nm thick silica layer grown on bulk amorphous silicon. By using a silicon layer underneath the 100 nm silica layer we prevent charging of the substrate during the CL measurement and the fabrication of the silica load with EBID. Each gold bar in the split-wire nanoantenna has the dimensions

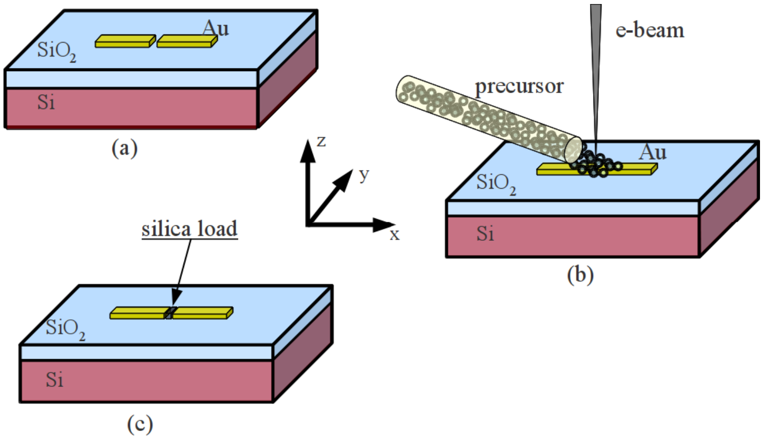

Figure 6.1: Schematic representation of the main steps towards obtaining loaded nanoantennas. (a) The gold split-wires are fabricated with electron beam lithography on top of a 100 nm thick silica substrate placed on a bulk silicon. (b) EBID is used to deposit silica to the gap region of the structures. (c) At the end of the process silica loaded split-wire nanoantennas are obtained ready for optical investigation.

100×100×400 nm. The gap between each bar is 30 nm (figure 6.2).

The split-wire nanoantennas are loaded by local deposition of silica with EBID. During the silica deposition between the nanoantennas, the chamber pressure is roughly 2.60×10^{-5} mbar. The deposition is performed with an 11 pA electron beam current at a 3 keV acceleration energy. A controlled movement of the electron beam along a track in the middle of the gap region of the split-wire nanoantenna ensures deposition in the gap only. The length of the track is 100 nm, i.e. equal to the width of the wires, oriented parallel to the *y axis* as indicated in figure 6.1. The amount of deposited material is varied by controlling the number of loops that the electron beam makes along the track. In order to observe the effect of the load we deposit with different electron doses, namely: 0, 3, 5, 7, 13, 17, 19, 23, 29, 37, 41, 47 and 57 nC/μm^2. The SEM micrographs of the resulting nanostructures comprising the nanoantennas with the loads in the gap regions are shown in figure 6.2. Figure 6.2*a* and 6.2*b* represent the nanoantennas without and with the smallest load, respectively. In figure 6.2*b* the load is hard to discern, whereas for higher doses the load is readily

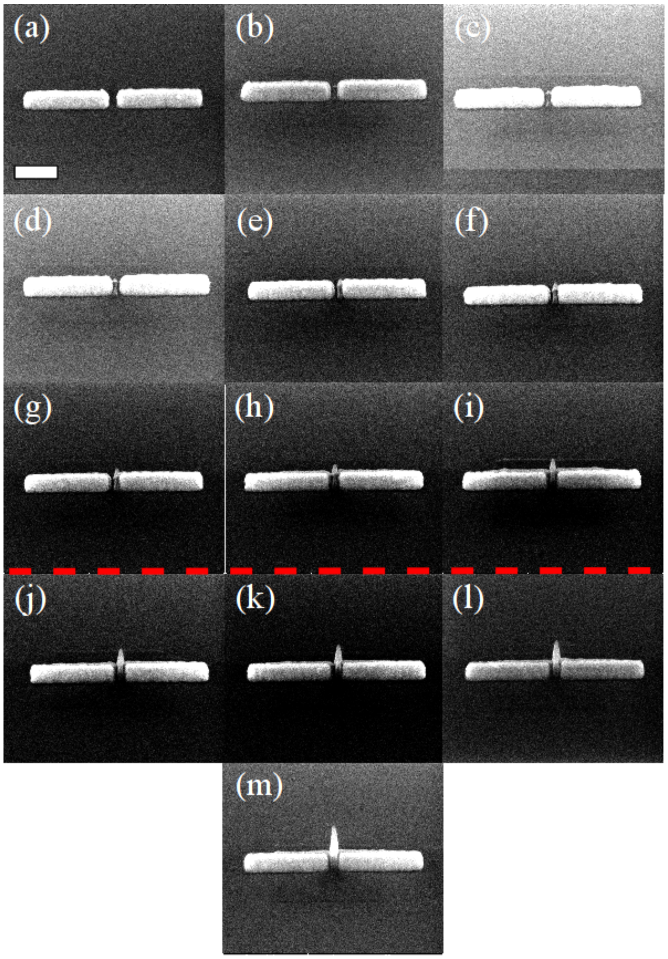

Figure 6.2: SEM micrographs of the split-wire nanoantennas (a) without and (b-m) with deposited silica in the gap region. Going from (b) to (m) the amount of deposition increases. All micrographs are taken at an angle of 52°*. The scale bar, seen in (a) (valid also for the rest) represents 200 nm. The red dashed line separates the nanoantennas for which the properties will be described with our heuristic model (see figure 6.6)*

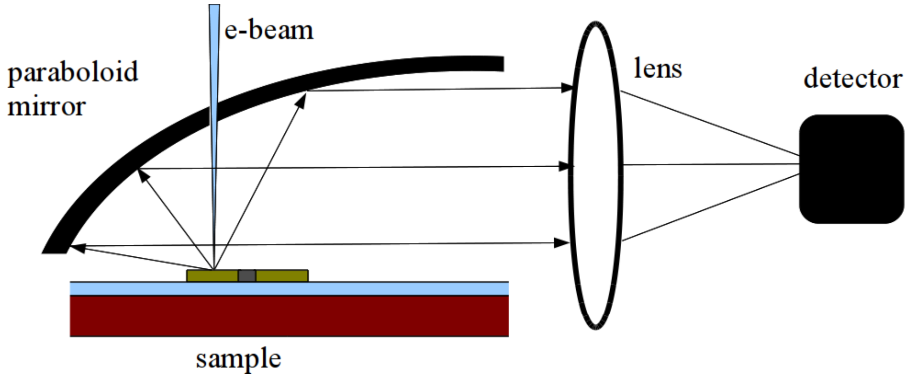

Figure 6.3: Schematic representation of the experimental (CL) setup. The focused electron beam with 30 keV scans the sample located at the focal point of the paraboloid mirror. The emitted photons are collected by the mirror and sent to the detector via a lens and a fiber (not shown).

observed. Comparing figures 6.2*c* through 6.2*g* it can be seen that the load is not always centered in the gap. We attribute these minor deviation to small drifts in the instrument. Starting from figure 6.2*h* the loads are extending from the gap field due to the relatively large amount of silica deposition.

Characterization of the split-wire nanoantennas is performed with CL spectroscopy. During the CL spectroscopy [179] the excitation of each nanoantenna is realized with a 30 keV focused electron beam performing a raster scan over the structure. The light emitted from the nanoantenna is collected by a paraboloid mirror which has a 4.6 sr acceptance angle. The light collected by the paraboloid mirror is focused onto 600 μm-diameter-core multimode fiber with an achromatic lens. The fiber is connected to a grating spectrometer (PI Acton SP2300i) with a liquid-nitrogen cooled CCD array. After the measurement process a CL excitation map is obtained. In figure 6.4 a CL excitation map that belongs an unloaded split-wire nanoantenna is presented. This typical measurement requires 3 minutes collection time. The measured wavelength for this graph is 805 nm with a 10 nm bin size. The color-scale denotes the collected amount of photons (normalized to the highest photon count). The dashed gray rectangles represent the location of the each nanobars of the split-wire nanoantenna. Figure 6.4 demonstrates the unique property of the CL technique. On one

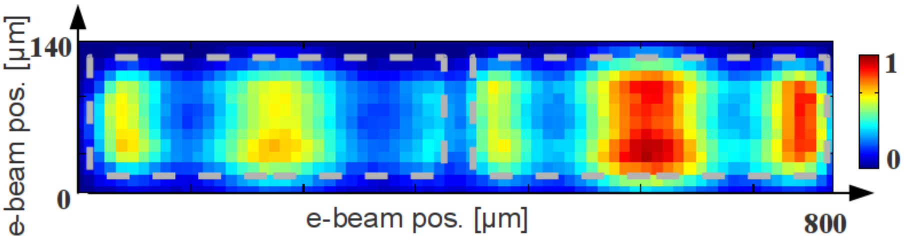

Figure 6.4: The excitation map of the split-wire nanoantenna without a load. Each pixel corresponds to the position of the electron beam. The gray dashed rectangles represent the location of the nanobars of the nanodipole. The color scale corresponds to photon count normalized to the highest value. The measured wavelength for this map is 805 nm.

hand the entire dimension of the excitation map is 800×140 nm^2, on the other hand the due to the local excitation property of the focused electron beam the resolution of the excitation map is as high as 10 nm. This resolution is roughly factor of 20 times higher with respect to an optical measurement performed with conventional far-field techniques. In other words, the CL technique enables us a local excitation of the nanostructures with deep sub-wavelength resolution. The pattern (figure 6.4) is an excitation pattern related to the local density of states of the structure [41, 180]. In a simplified picture the pattern can, to a certain extent, be regarded as a high resolution snapshot of the local field distribution of an excited split-wire nanoantenna. The overall picture reveals a roughly periodic pattern of nodes and anti-nodes along the horizontal axis of the excitation map. The pattern is similar to the one obtained in the near-field with a scanning near-field optical microscopy [181] and in the far-field with two photon luminescence technique [182].

6.3 Results and discussion

In order to observe the effect of the loading CL spectroscopy is performed for all split-wire nanoantennas loaded with different amounts of silica. The measured spectra of all structures is shown in figure 6.5. All spectra of the nanoantennas, loaded and unloaded, exhibit a single broad peak in the investigated wavelength range. The peak width is 50 nm [full width

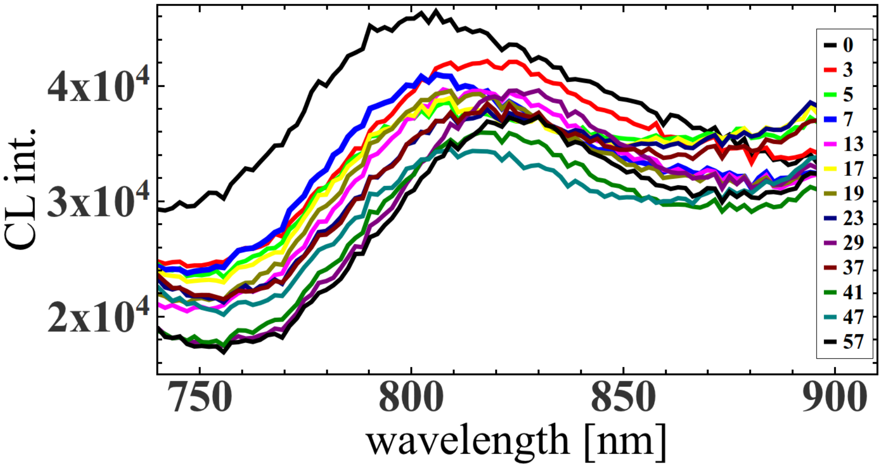

Figure 6.5: The measured CL spectrum of the nanodipole antennas loaded with various amount of silica in the gap region. The legend in the graph includes the dose values (in nC/μm^2) used for the silica deposition.

at half maximum (FWHM)] for all nanoantennas. With the increasing loading the CL intensity drops, while the overall shapes of the spectra stay the same. The intensity drop is largest when going from no load to the smallest load. In addition the resonance peaks shift towards the longer wavelengths. The peaks shift in a wavelength range between 805 and 825 nm. We determine the peak positions in each graph by fitting a polynomial function to the spectrum of each split-wire nanoantenna. Figure 6.6 represents the resonance position of each nanoantenna as a function of the electron dose. The blue line is a guide to eye and represents the trend of the resonance peak with loading for the smallest doses. The error bars in the resonance and dose axes are estimated from the uncertainties in the length of the nanoantennas and in the amount deposited material, respectively. Please note that length variations and the concomitant peak shifts represent a larger uncertainty than the determination of the peak positions through the peak fitting.

In the following we will describe the behavior of the nanoantennas with a heuristic model based on first-order perturbation theory. Please note that we will only describe the behavior of the doses less than or equal to 29 nC/μm^2, i.e. structures above the red dashed line in figure 6.2 and left

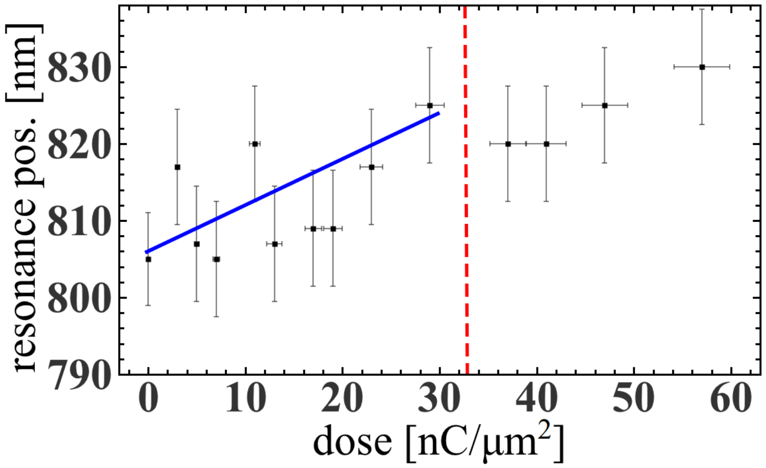

Figure 6.6: The resonance position of the loaded split-wire nanoantennas as a function of the electron dose of the EBID. The first nine antennas (at the right hand side of the red dashed line) are used in the analysis. The resonance wavelength shifts towards red with the increasing load.

of the red dashed line in figure 6.6. The reason for this selection lies in the spatial distribution of the electric field in the gap region. Calculations [183] for the split-wire nanoantennas indicate that the confinement of the electric field in the nanocavity occurs within the volume of the gap region in between the metal nanobars. The magnitude of the electric field exponentially decreases away from the gap. Hence, beyond a certain distance and therefore height of the deposit, there would be no effective interaction between the deposited material and electric field in the gap region. In fact this effect also can be seen in our data. The comparison of the trends between the left and right hand side of the red line in figure 6.6 points that after a certain amount of deposition (dose of 29 nC/μm^2) the red shift seems to saturate.

Experimentally and numerically [181, 183] it was shown that small perturbations in the gap region of the nanoantennas can cause a change in the optical response of the whole resonant system that can be used for sensing and trapping purposes [184]. Thus, the optical response of the whole system can be explained in terms of the perturbations in the gap region as the electric field is far stronger inside the gap than outside. For small perturbations we will treat the split-wire nanoantenna as if the gap region is a nanocavity. The optical response of photonic crystal nanocavities under small perturbations has been investigated by using metallic and/or dielectric near-field probes both theoretically [185] and experimentally [186, 187]. We use the same methodology to describe the behavior of the split-wire nanoantennas. According to the perturbation theory, while neglecting the magnetic contribution [188, 189], the wavelength shift in terms of the load in the gaps can be written as [187]

$$\frac{\Delta\lambda_0}{\lambda_0} = \frac{\mathbf{E}_0^* \cdot \mathbf{p}}{2U_E}, \tag{6.3.0.1}$$

where $\Delta\lambda_0$ corresponds to the wavelength shift, $\mathbf{E}_0$ is the unperturbed electric field, $U_E = (\varepsilon_0/2)\int d^3\mathbf{x}|\mathbf{E}_0|^2$ is the stored energy in the system. The electric dipole moment $\mathbf{p}$ is expressed as $\mathbf{p} = \alpha_e \mathbf{E}_0$ where α_e, the electric polarizability of the deposited material in the gap. Here it is assumed that the electric field, $\mathbf{E}_0$, is uniform (constant) in the cavity, which is why we only use this model to describe the behavior for small doses for which the deposit is located in the gap [185]). The electric polarizability —with electrostatic approximation for particles that are small compared to the wavelength— can be obtained as follows [190, 191]:

$$\alpha_e = 3(\frac{\epsilon_m - 1}{\epsilon_m + 2})V_{eff}, \tag{6.3.0.2}$$

where ϵ_m and V_{eff} are the dielectric constant and the effective volume of the loaded material in the gap, respectively. The formula is also known as "Waldron's formula" [192]. In microwave and rf engineering it is used for tuning transmission lines, measurement of a material's dielectric constant inside a cavity and measuring the frequency shift [193]. The fact that the polarizability depends on the volume of the dielectric material in the nanocavity qualitatively explains the red shift of the nanoantenna which increases with increasing dose.

We assume that the molar mass of the deposit is equal to that of bulk silica (2.65 gr/cm^3). In addition, and from the SEM micrographs of deposited materials the volume of the deposited materials can be deduced. Thus, the wavelength shift can be found as a function of the mass of the deposited silica. The plot in figure 6.7 represents the resonance shift of the nanoantennas as a function of the mass of the deposited material. The

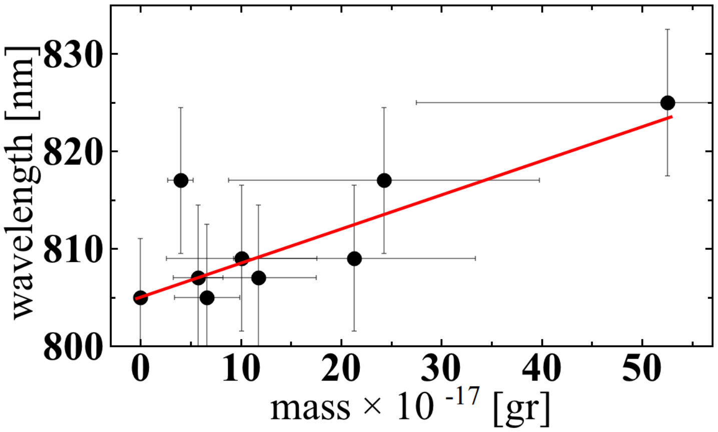

Figure 6.7: The sensitivity of the split-wire nanoantenna in terms of the mass of the deposited material in the gap.

error bars in the mass axis stem from the volume uncertainty of the silica loads as determined from the SEM micrographs. The slope of the nine data points gives the sensitivity of the nanoantennas in terms of the mass that is equal to 2.5×10^{-19} gr/nm.

6.4 Conclusion

We show that the local deposition feature of EBID can be exploited to load the gap of the metallic split-wire nanoantennas with a dielectric material (silica). The optical measurement —with CL spectroscopy— of the individual split-wire nanoantennas shows that the resonance wavelength shifts towards the longer wavelengths depending on to the amount of deposited silica in the gap region. EBID is a therefore versatile nanostructuring method for controlling and passively tuning the optical frequencies of the nanophotonic devices without changing the length and/or geometry. The possibility to deposit different materials (see Chapter 2), such as semiconductors, in the gap paves the way for active control of nanoantennas [176] which is of interest for optical switching and quantum information technology.

References

[1] L. Novotny and B. Hecht, *Principles of Nano-Optics* (Cambridge University Press, 2008).

[2] I. A. Sukhoivanov and I. V. Guryev, *Photonic Crystals: Physics and Practical Modeling* (Springer Series in Optical Sciences, 2009).

[3] L. Rayleigh, *On the maintenance of vibrations by forces of double frequency, and on the propagation of waves through a medium endowed with a periodic structure*, Philosophical Magazine Series 5 **24**, 145 (1887).

[4] J. E. G. J. Wijnhoven and W. L. Vos, *Preparation of Photonic Crystals Made of Air Spheres in Titania*, Science **281**, 802 (1998).

[5] T. F. Krauss, R. M. D. L. Rue, and S. Brand, *Two-dimensional photonic-bandgap structures operating at near-infrared wavelengths*, Nature **383**, 699 (1996).

[6] Blanco, E. Chomski, S. Grabtchak, M. Ibisate, S. John, S. Leonard, C. Lopez, F. Meseguer, H. Miguez, J. Mondia, G. Ozin, O. Toader, and van Driel HM, *Large-scale synthesis of a silicon photonic crystal with a complete three-dimensional bandgap near 1.5 micrometres*, Nature **405**, 437 (2000).

[7] V. P. Bykov, *Spontaneous emission in a periodic structures*, J. Exp. Theor. Phys. **35**, 269 (1972).

[8] E. Yablonovitch, *Inhibited Spontaneous Emission in Solid-State Physics and Electronics*, Phys. Rev. Lett. **58**, 2059 (1987).

[9] S. John, *Strong localization of photons in certain disordered dielectric superlattices*, Phys. Rev. Lett. **58**, 2486 (1987).

[10] K. M. Ho, C. T. Chan, and C. M. Soukoulis, *Existence of a photonic gap in periodic dielectric structures*, Phys. Rev. Lett. **65**, 3152 (1990).

[11] H. S. Sözüer, J. W. Haus, and R. Inguva, *Photonic bands: Convergence problems with the plane-wave method*, Phys. Rev. B **45**, 13962 (1992).

[12] A. V. Zayats, I. I. Smolyaninov, and A. A. Maradudin, *Nano-optics of surface plasmon polaritons*, Physics Reports **408**, 131 (2005).

[13] S. A. Maier and H. A. Atwater, *Plasmonics: Localization and guiding of electromagnetic energy in metal/dielectric structures*, Journal of Applied Physics **98**, 011101 (2005).

[14] G. Mie, *Beitraege zur Optik trüber Medien, speziell kolloidaler Metalloesungen*, Annalen der Physik **330**, 377 (1908).

[15] R. H. Ritchie, *Plasma Losses by Fast Electrons in Thin Films*, Phys. Rev. **106**, 874 (1957).

[16] D. A. Weitz, S. Garoff, J. I. Gersten, and A. Nitzan, *The enhancement of Raman scattering, resonance Raman scattering, and fluorescence from molecules adsorbed on a rough silver surface*, The Journal of Chemical Physics **78**, 5324 (1983).

[17] M. Kerker, D.-S. Wang, and H. Chew, *Surface enhanced Raman scattering (SERS) by molecules adsorbed at spherical particles: errata*, Appl. Opt. **19**, 4159 (1980).

[18] P. C. Lee and D. Meisel, *Adsorption and surface-enhanced Raman of dyes on silver and gold sols*, The Journal of Physical Chemistry **86**, 339 (1982).

[19] T. W. Ebbesen, H. J. Lezec, H. F. Ghaemi, T. Thio, and P. A. Wolff, *Extraordinary optical transmission through sub-wavelength hole arrays*, Nature **391**, 667 (1998).

[20] F. J. Garcia-Vidal, L. Martin-Moreno, T. W. Ebbesen, and L. Kuipers, *Light passing through subwavelength apertures*, Rev. Mod. Phys. **82**, 729 (2010).

[21] J.-C. Weeber, J. R. Krenn, A. Dereux, B. Lamprecht, Y. Lacroute, and J. P. Goudonnet, *Near-field observation of surface plasmon polariton propagation on thin metal stripes*, Phys. Rev. B **64**, 045411 (2001).

[22] R. Charbonneau, P. Berini, E. Berolo, and E. Lisicka-Shrzek, *Experimental observation of plasmon polariton waves supported by a thin metal film of finite width*, Opt. Lett. **25**, 844 (2000).

[23] K. Su, Q. Wei, X. Zhang, J. Mock, D. Smith, and S. Schultz, *Interparticle coupling effects on plasmon resonances of nanogold particles*, Nano Letters **3**, 1087 (2003).

[24] F. Tam, C. Moran, and N. Halas, *Geometrical Parameters Controlling Sensitivity of Nanoshell Plasmon Resonances to Changes in Dielectric Environment*, J.Phys. Chem. B **108**, 17290 (2004).

[25] G. Raschke, S. Brogl, A. S. Susha, A. L. Rogach, T. A. Klar, J. Feldmann, B. Fieres, N. Petkov, T. Bein, A. Nichtl, and K. Krzinger, *Gold Nanoshells Improve Single Nanoparticle Molecular Sensors*, Nano Letters **4**, 1853 (2004).

[26] E. Dulkeith, A. C. Morteani, T. Niedereichholz, T. A. Klar, J. Feldmann, S. A. Levi, F. C. J. M. van Veggel, D. N. Reinhoudt, M. Möller, and D. I. Gittins, *Fluorescence Quenching of Dye Molecules near Gold Nanoparticles: Radiative and Nonradiative Effects*, Phys. Rev. Lett. **89**, 203002 (2002).

[27] S. Jetté-Charbonneau, R. Charbonneau, N. Lahoud, G. Mattiussi, and P. Berini, *Demonstration of Bragg gratings based on long-ranging surface plasmon polariton waveguides*, Opt. Express **13**, 4674 (2005).

[28] J. G. Rivas, M. Kuttge, P. H. Bolivar, H. Kurz, and J. A. Sánchez-Gil, *Propagation of surface plasmon polaritons on semiconductor gratings*, Phys. Rev. Lett. **93**, 256804 (2004).

[29] R. Feynman, *There's plenty of room at the bottom [data storage]*, Journal of Microelectromechanical Systems, **1**, 60 (1992).

[30] R. Feynman, *Infinitesimal machinery*, Journal of Microelectromechanical Systems, **2**, 4 (1993).

[31] D. M. Beggs, T. F. Krauss, L. Kuipers, and T. Kampfrath, *Ultrafast tilting of the dispersion of a photonic crystal and adiabatic spectral compression of light pulses*, Phys. Rev. Lett. **108**, 033902 (2012).

[32] L. A. Woldering, A. Otter, B. H. Husken, and W. L. Vos, *Focused ion beam milling of nanocavities in single colloidal particles and self-assembled opals*, Nanotechnology **17**, 5717 (2006).

[33] L. A. Woldering, R. W. Tjerkstra, H. V. Jansen, I. D. Setija, and W. L. Vos, *Periodic arrays of deep nanopores made in silicon with reactive ion etching and deep UV lithography*, Nanotechnology **19**, 1 (2008).

[34] G. A. Ozin and S. M. Yang, *The race for the photonic chip: colloidal crystal assembly in silicon wafers*, Advanced Functional Materials **11**, 95 (2001).

[35] O. L. Muskens, S. L. Diedenhofen, B. C. Kaas, R. E. Algra, E. P. A. M. Bakkers, J. Gomez Rivas, and A. Lagendijk, *Large photonic strength of highly tunable resonant nanowire materials*, Nano Letters **9**, 930 (2009).

[36] S. L. Diedenhofen, O. T. A. Janssen, G. Grzela, E. P. A. M. Bakkers, and J. Gmez Rivas, *Strong geometrical dependence of the absorption of light in arrays of semiconductor nanowires*, ACS Nano **5**, 2316 (2011).

[37] M. A. Verschuuren, P. Gerlach, H. A. van Sprang, and A. Polman, *Improved performance of polarization-stable VCSELs by monolithic sub-wavelength gratings produced by soft nano-imprint lithography*, Nanotechnology **22**, 505201 (2011).

[38] M. Burresi, D. van Oosten, T. Kampfrath, H. Schoenmaker, R. Heideman, A. Leinse, and L. Kuipers, *Probing the magnetic field of light at optical frequencies*, Science **326**, 550 (2009).

[39] B. Hecht, B. Sick, U. P. Wild, V. Deckert, R. Zenobi, O. J. F. Martin, and D. W. Pohl, *Scanning near-field optical microscopy with aperture probes: Fundamentals and applications*, The Journal of Chemical Physics **112**, 7761 (2000).

[40] D. Drews, W. Ehrfeld, M. Lacher, K. Mayr, W. Noell, S. Schmitt, and M. Abraham, *Nanostructured probes for scanning near-field optical microscopy*, Nanotechnology **10**, 61 (1999).

[41] E. J. R. Vesseur, T. Coenen, H. Caglayan, N. Engheta, and A. Polman, *Experimental Verification of* $n = 0$ *Structures for Visible Light*, Phys. Rev. Lett. **110**, 013902 (2013).

[42] J. Bertolotti, E. van Putten, C. Blum, A. Lagendijk, W. Vos, and A. P. Mosk, *Non-invasive imaging through opaque scattering layers*, Nature **491**, 232–234 (2012), fulltext.

[43] Y. Chen, K. Munechika, and D. S. Ginger, *Dependence of Fluorescence Intensity on the Spectral Overlap between Fluorophores and Plasmon Resonant Single Silver Nanoparticles*, Nano Letters **7**, 690 (2007).

[44] I. Sersic, C. Tuambilangana, and A. F. Koenderink, *Fourier microscopy of single plasmonic scatterers*, New Journal of Physics **13**, 083019 (2011).

[45] L. A. Giannuzzi and F. A. Stevie, *Introduction to focused ion beams instrumentation, theory, techniques, and practice* (Springer, 2005).

[46] S. J. Randolph, J. D. Fowlkes, and P. D. Rack, *Focused, Nanoscale Electron-Beam-Induced Deposition and Etching*, Crit. Rev. Solid State Mater. Sci. **31**, 55 (2006).

[47] S. Matsui, *Focused-ion-beam deposition for 3-D nanostructure fabrication*, Nuclear Instruments and Methods in Physics Research Section B: Beam Interactions with Materials and Atoms **257**, 758 (2007).

[48] W. F. van Dorp, B. van Someren, C. W. Hagen, P. Kruit, and P. A. Crozier, *Approaching the Resolution Limit of Nanometer-Scale Electron Beam-Induced Deposition*, Nano Letters **5**, 1303 (2005).

[49] J. C. van Oven, F. Berwald, K. K. Berggren, P. Kruit, and C. W. Hagen, *Electron-beam-induced deposition of 3-nm-half-pitch patterns on bulk Si*, Journal of Vacuum Science & Technology B: Microelectronics and Nanometer Structures **29**, 06F305 (2011).

[50] S. Graells, S. Aimovi, G. Volpe, and R. Quidant, *Direct Growth of Optical Antennas Using E-Beam-Induced Gold Deposition*, Plasmonics **5**, 135 (2010), 10.1007/s11468-010-9128-9.

[51] A. Botman, J. J. L. Mulders, R. Weemaes, and S. Mentink, *Purification of platinum and gold structures after electron-beam-induced deposition*, Nanotechnology **17**, 3779 (2006).

[52] P. Kruit, *The first international workshop on EBID, (unpublished)* (Delft University of Technology, 2006).

[53] J. D. Beard and S. N. Gordeev, *Fabrication and Buckling Dynamics of Nanoneedle AFM probes*, Nanotechnology **22**, 175303 (2011).

[54] F. Hernandez-Ramirez, A. Tarancon, O. Casals, J. Rodriguez, A. Romano-Rodriguez, J. R. Morante, S. Barth, S. Mathur, T. Y. Choi, D. Poulikakos, V. Callegari, and P. M. Nellen, *Fabrication and electrical characterization of circuits based on individual tin oxide nanowires*, Nanotechnology **17**, 5577 (2006).

[55] H. Acar, T. Coenen, A. Polman, and L. K. Kuipers, *Dispersive Ground Plane CoreShell Type Optical Monopole Antennas Fabricated with Electron Beam Induced Deposition*, ACS Nano **6**, 8226 (2012).

[56] E. Ruska, *The development of the electron microscope and of electron microscopy*, Rev. Mod. Phys. **59**, 627 (1987).

[57] R. L. Stewart, *Insulating Films Formed Under Electron and Ion Bombardment*, Phys. Rev. **45**, 488 (1934).

[58] A. Ennos, *The sources of electron-induced contamination in kinetic vacuum systems*, Br. J. Appl. Phys **4**, 101 (1953).

[59] K. M. Poole, *Electrode Contamination in Electron Optical Systems*, Proceedings of the Physical Society. Section B **66**, 542 (1953).

[60] A. G. Baker and W. C. Morris, *Deposition of Metallic Films by Electron Impact Decomposition of Organometallic Vapors*, Review of Scientific Instruments **32**, 458 (1961).

[61] R. K. Hart, T. F. Kassner, and J. K. Maurin, *The contamination of surfaces during high-energy electron irradiation*, Philosophical Magazine **21**, 453 (1970).

[62] D. A. Smith, J. D. Fowlkes, and P. D. Rack, *Understanding the Kinetics and Nanoscale Morphology of Electron-Beam-Induced Deposition via a Three-Dimensional Monte Carlo Simulation: The Effects of the Precursor Molecule and the Deposited Material*, Small **4**, 1382 (2008).

[63] I. Utke, P. Hoffmann, and J. Melngailis, *Gas-assisted focused electron beam and ion beam processing and fabrication*, Journal of Vacuum Science & Technology B: Microelectronics and Nanometer Structures **26**, 1197 (2008).

[64] L. Reimer and D. Stelter, *FORTRAN 77 monte-carlo program for minicomputers using mott cross-sections*, Scanning **8**, 265 (1986).

[65] D. Drouin, A. R. Couture, D. Joly, X. Tastet, V. Aimez, and R. Gauvin, *CASINO V2.42A Fast and Easy-to-use Modeling Tool for Scanning Electron Microscopy and Microanalysis Users*, Scanning **29**, 92 (2007).

[66] W. F. van Dorp and C. W. Hagen, *A critical literature review of focused electron beam induced deposition*, Journal of Applied Physics **104**, 081301 (2008).

[67] P.Hoffmann, *The first international workshop on EBID, (unpublished)* (Delft University of Technology, 2006).

[68] H. W. P. Koops, R. Weiel, D. P. Kern, and T. H. Baum, *High-resolution electron-beam induced deposition*, Journal of Vacuum Science & Technology B: Microelectronics and Nanometer Structures **6**, 477 (1988).

[69] A. Ishibashi, K. Funato, and Y. Mori, *Electron-beam-induced resist and aluminum formation*, Journal of Vacuum Science & Technology B: Microelectronics and Nanometer Structures **9**, 169 (1991).

[70] J. Fujita, M. Ishida, T. Ichihashi, Y. Ochiai, T. Kaito, and S. Matsui, *Carbon nanopillar laterally grown with electron beam-induced chemical vapor deposition*, Journal of Vacuum Science & Technology B: Microelectronics and Nanometer Structures **21**, 2990 (2003).

[71] T. Takahashi, Y. Arakawa, M. Nishioka, and T. Ikoma, *Selective growth of GaAs wire structures by electron beam induced metalorganic chemical vapor deposition*, Applied Physics Letters **60**, 68 (1992).

[72] S. Matsui and M. Mito, *Si deposition by electron beam induced surface reaction*, Applied Physics Letters **53**, 1492 (1988).

[73] B. H. Chin and G. Ehrlich, *Formation of silicon nitride structures by direct electron beam writing*, Applied Physics Letters **38**, 253 (1981).

[74] S. Lipp, L. Frey, C. Lehrer, B. Frank, E. Demm, S. Pauthner, and H. Ryssel, *Tetramethoxysilane as a precursor for focused ion beam and electron beam assisted insulator (SiOx) deposition* (AVS, 1996), No. 6, pp. 3920–3923.

[75] W. J. Mitchell and E. L. Hu, *Selective area chemical vapor deposition of titanium oxide films: Characterization of* $Ti(OC_3H_7)_4$ *as an electron beam resist* (AVS, 1999), No. 4, pp. 1622–1626.

[76] S. J. Randolph, J. D. Fowlkes, and P. D. Rack, *Focused, Nanoscale Electron-Beam-Induced Deposition and Etching*, Critical Reviews in Solid State and Materials Sciences **31**, 55 (2006).

[77] V. Friedli and I. Utke, *Optimized molecule supply from nozzle-based gas injection systems for focused electron- and ion-beam induced deposition and etching: simulation and experiment*, Journal of Physics D: Applied Physics **42**, 125305 (2009).

[78] P. A. Crozier, J. Tolle, J. Kouvetakis, and C. Ritter, *Synthesis of uniform GaN quantum dot arrays via electron nanolithography of* D_2GaN_3, Applied Physics Letters **84**, 3441 (2004).

[79] N. Silvis-Cividjian, C. W. Hagen, P. Kruit, M. A. J. v.d. Stam, and H. B. Groen, *Direct fabrication of nanowires in an electron microscope*, Applied Physics Letters **82**, 3514 (2003).

[80] S. Matsui and K. Mori, *New selective deposition technology by electron-beam induced surface reaction*, Journal of Vacuum Science & Technology B: Microelectronics and Nanometer Structures **4**, 299 (1986).

[81] *Nanofabrication Using Focused Ion and Electron Beams - Principles and Applications*, edited by I. Utke, S. Moshkalev, and P. Russell (Oxford University Press, 2011), pp. 127–132.

[82] *The gas injector system for SEM and DualBeam*, FEI.

[83] J. J. L. Mulders, *The first international workshop on EBID, (unpublished)* (Delft University of Technology, 2006).

[84] K. Kohlmann, M. Thiemann, and W. Brünger, *E-beam induced X-ray mask repair with optimized gas nozzle geometry*, Microelectronic Engineering **13**, 279 (1991).

[85] F. Rugamas, D. Roundy, G. Mikaelian, G. Vitug, M. Rudner, J. Shih, D. Smith, J. Segura, and M. A. Khakoo, *Angular profiles of molecular beams from effusive tube sources: I. Experiment*, Measurement Science and Technology **11**, 1750 (2000).

[86] L. Reimer, *Scanning electron microscopy* (Springer-Verlag, 1998).

[87] P. M. George and J. Beauchamp, *Deposition of metal films by the controlled decomposition of organometallic compounds on surfaces*, Thin Solid Films **67**, L25 (1980).

[88] N. Silvis-Cividjian, C. Hagen, L. Leunissen, and P. Kruit, *The role of secondary electrons in electron-beam-induced-deposition spatial resolution*, Microelectronic Engineering **6162**, 693 (2002).

[89] J. D. Fowlkes, S. J. Randolph, and P. D. Rack, *Growth and simulation of high-aspect ratio nanopillars by primary and secondary electron-induced deposition* (AVS, 2005), No. 6, pp. 2825–2832.

[90] N. Tesla, *Method of and appartus for controlling mechanism of moving vessels or vehicles*, U. S. Patent 613809 (1898).

[91] L. Novotny and N. van Hulst, *Antennas for Light*, Nat. Photonics **5**, 83 (2011).

[92] V. Giannini, A. I. Fernandez-Dominguez, S. C. Heck, and S. A. Maier, *Plasmonic Nanoantennas: Fundamentals and Their Use in Controlling the Radiative Properties of Nanoemitters*, Chemical Reviews **111**, 3888 (2011).

[93] A. Balanis, *Antenna Theory Analysis and Design*, 3rd ed. (Wiley-Interscience, 2005).

[94] C. David and F. J. García de Abajo, *Spatial Nonlocality in the Optical Response of Metal Nanoparticles*, J. Phys. Chem. C **115**, 19470 (2011).

[95] M. Hentschel, M. Schoeferling, T. Weiss, N. Liu, and H. Giessen, *Three-Dimensional Chiral Plasmonic Oligomers*, Nano Lett. **12**, 2542 (2012).

[96] A. G. Curto, G. Volpe, T. H. Taminiau, M. P. Kreuzer, R. Quidant, and N. F. van Hulst, *Unidirectional Emission of a Quantum Dot Coupled to a Nanoantenna*, Science **329**, 930 (2010).

[97] B. Deutsch, R. Hillenbrand, and L. Novotny, *Visualizing the Optical Interaction Tensor of a Gold Nanoparticle Pair*, Nano Lett. **10**, 652 (2010).

[98] N. Djaker, R. Hostein, E. Devaux, T. W. Ebbesen, H. Rigneault, and J. Wenger, *Surface Enhanced Raman Scattering on a Single Nanometric Aperture*, J. Phys. Chem. C **114**, 16250 (2010).

[99] H. A. Atwater and A. Polman, *Plasmonics or Improved Photovoltaic Devices*, Nat. Mater. **9**, 205 (2010).

[100] S. Thongrattanasiri, F. H. L. Koppens, and F. J. García de Abajo, *Complete Optical Absorption in Periodically Patterned Graphene*, Phys. Rev. Lett. **108**, 047401 (2012).

[101] Y. C. Jun, K. C. Huang, and M. L. Brongersma, *Plasmonic Beaming and Active Control over Fluorescent Emission*, Nat. Commun. **2**, 283 (2011).

[102] T. Coenen, E. J. R. Vesseur, and A. Polman, *Angle-Resolved Cathodoluminescence Spectroscopy*, Appl. Phys. Lett. **99**, 143103 (2011).

[103] T. Coenen, E. J. R. Vesseur, A. Polman, and A. F. Koenderink, *Directional Emission from Plasmonic Yagi-Uda Antennas Probed by Angle-Resolved Cathodoluminescence Spectroscopy*, Nano Lett. **11**, 3779 (2011).

[104] W. F. van Dorp and C. W. Hagen, *A critical Literature Review of Focused Electron Beam Induced Deposition*, J. Appl. Phys. **104**, 081301 (2008).

[105] E. D. Palik, *Handbook of Optical Constants* (Academy Press, 1985).

[106] L. Novotny, *Effective Wavelenth Scaling for Optical Antennas*, Phys. Rev. Letters **98**, 266802 (2007).

[107] T. H. Taminiau, F. D. Stefani, and N. F. van Hulst, *Optical Nanorod Antennas Modelled as Cavities for Dipolar Emitters:Evolution of Sub- and Super-Radiant Modes*, Nano Lett. **11**, 1020 (2011).

[108] A. Sommerfeld, *Uber die Fortpflanzung Elektrodynamischer Wellen Langs Eines Drahtes*, Ann. Physik (Berlin) **303**, 233 (1899).

[109] E. Cubukcu and F. Capasso, *Optical Nanorod Antennas as Dispersive One-Dimensional Fabry-Perot Resonators for Surface Plasmons*, Appl. Phys. Lett. **95**, 201101 (2009).

[110] N. S. King, Y. Li, C. Ayala-Orozco, T. Brannan, P. Nordlander, and N. J. Halas, *Angle- and Spectral-Dependent Light Scattering from Plasmonic Nanocups*, Nano Lett. **5**, 7254 (2011).

[111] Y. Zhang, A. Barhoumi, J. B. Lassiter, and N. J. Halas, *Orientation-Preserving Transfer and Directional Light Scattering from Individual Light-Bending Nanoparticles*, Nano Lett. **11**, 1838 (2011).

[112] A. Alú and N. Engheta, *Tuning the Scattering Response of Optical Nanoantennas with Nanocircuit Loads*, Nat. Photonics **2**, 307 (2008).

[113] C. M. Soukoulis and M. Wegener, *Past achievements and future challenges in the development of three-dimensional photonic metamaterials*, Nat. Photonics **5**, 523 (2011).

[114] R. A. Shelby, D. R. Smith, and S. Schultz, *Experimental Verification of a Negative Index of Refraction*, Science **292**, 77 (2001).

[115] D. Schurig, J. J. Mock, B. J. Justice, S. A. Cummer, J. B. Pendry, A. F. Starr, and D. R. Smith, *Metamaterial Electromagnetic Cloak at Microwave Frequencies*, Science **314**, 977 (2006).

[116] N. Liu, H. Guo, L. Fu, S. Kaiser, H. Schweizer, and H. Giessen, *Three-dimensional photonic metamaterials at optical frequencies*, Nat Mater **7**, 31 (2008).

[117] K. Hoeflich, R. B. Yang, A. Berger, G. Leuchs, and S. Christiansen, *The Direct Writing of Plasmonic Gold Nanostructures by Electron-Beam-Induced Deposition*, Advanced Materials **23**, 2657 (2011).

[118] J. A. Fan, C. Wu, K. Bao, J. Bao, R. Bardhan, N. J. Halas, V. N. Manoharan, P. Nordlander, G. Shvets, and F. Capasso, *Self-Assembled Plasmonic Nanoparticle Clusters*, Science **328**, 1135 (2010).

[119] R. J. Macfarlane, B. Lee, M. R. Jones, N. Harris, G. C. Schatz, and C. A. Mirkin, *Nanoparticle Superlattice Engineering with DNA*, Science **334**, 204 (2011).

[120] N. C. Seeman, *Nanomaterials Based on DNA*, Annual Review of Biochemistry **79**, 65 (2010).

[121] P. W. K. Rothemund, *Folding DNA to create nanoscale shapes and patterns*, Nature **440**, 297 (2006).

[122] S. M. Douglas, H. Dietz, T. Liedl, B. Hogberg, F. Graf, and W. M. Shih, *Self-assembly of DNA into nanoscale three-dimensional shapes*, Nature **459**, 414 (2009).

[123] W. Yan, L. Xu, C. Xu, W. Ma, H. Kuang, L. Wang, and N. A. Kotov, *Self-Assembly of Chiral Nanoparticle Pyramids with Strong R/S Optical Activity*, Journal of the American Chemical Society **134**, 15114 (2012).

[124] A. Kuzyk, R. Schreiber, Z. Fan, G. Pardatscher, E. Roller, A. Hgele, F. Simmel, A. Govorov, and T. Liedl, *DNA-based self-assembly of chiral plasmonic nanostructures with tailored optical response.*, Nature **483**, 311 (2012).

[125] J. K. Gansel, M. Thiel, M. S. Rill, M. Decker, K. Bade, V. Saile, G. von Freymann, S. Linden, and M. Wegener, *Gold Helix Photonic Metamaterial as Broadband Circular Polarizer*, Science **325**, 1513 (2009).

[126] S. Kawata, H. B. Sun, T. Tanaka, and K. Takada, *Finer features for functional microdevices.*, Nature **412**, 697 (2001).

[127] M. Deubel, G. von Freymann, M. Wegener, S. Pereira, K. Busch, and C. M. Soukoulis, *Direct laser writing of three-dimensional photonic-crystal templates for telecommunications*, Nat. Mater. **3**, 444 (2004).

[128] J. Fischer, G. von Freymann, and M. Wegener, *The Materials Challenge in Diffraction-Unlimited Direct-Laser-Writing Optical Lithography*, Advanced Materials **22**, 3578 (2010).

[129] C. Helgert, E. Pshenay-Severin, M. Falkner, C. Menzel, C. Rockstuhl, E.-B. Kley, A. Tnnermann, F. Lederer, and T. Pertsch, *Chiral Metamaterial Composed of Three-Dimensional Plasmonic Nanostructures*, Nano Letters **11**, 4400 (2011).

[130] M. Hentschel, M. Schaeferling, T. Weiss, N. Liu, and H. Giessen, *Three-Dimensional Chiral Plasmonic Oligomers*, Nano Letters **12**, 2542 (2012).

[131] H. D. Wanzenboeck (unpublished).

[132] D. N. Stacey, *Experiments on the Electro-Weak Interaction in Atoms*, Physica Scripta **1992**, 15 (1992).

[133] D. K. Kondepudi and D. J. Durand, *Chiral asymmetry in spiral galaxies?*, Chirality **13**, 351 (2001).

[134] J. F. Nye, *Physical Properties of Crystals* (Oxford University Press, 1961).

[135] A. Sommerfeld, *Optics* (Academic Press, New York,, 1964).

[136] L. Pasteur, , Ann. Chim. Phys. **24**, 442 (1848).

[137] V. Prelog (unpublished).

[138] G. H. Wagniere, *On Chirality and the Universal Asymmetry-Reflections on Image and Mirror Image* (Wiley-VCH, 2007).

[139] G. P. Moss, *Basic terminology of stereochemistry*, Pure Appl. Chem **68**, 2193 (1996).

[140] G. Shemer, O. Krichevski, G. Markovich, T. Molotsky, I. Lubitz, and A. B. Kotlyar, *Chirality of Silver Nanoparticles Synthesized on DNA*, Journal of the American Chemical Society **128**, 11006 (2006).

[141] Y. Tang and A. E. Cohen, *Optical Chirality and Its Interaction with Matter*, Phys. Rev. Lett. **104**, 163901 (2010).

[142] W. A. Bonner, *Parity violation and the evolution of biomolecular homochirality*, Chirality **12**, 114 (2000).

[143] J. March, *Advanced Organic Chemistry: Reactions, Mechanisms, and Structure, 3rd ed.* (New York: Wiley, 1985).

[144] E. Shamonina and L. Solymar, *Metamaterials: How the subject started*, Metamaterials **1**, 12 (2007).

[145] B. Wang, J. Zhou, T. Koschny, M. Kafesaki, and C. M. Soukoulis, *Chiral metamaterials: simulations and experiments*, Journal of Optics A: Pure and Applied Optics **11**, 114003 (2009).

[146] S. Tretyakov, I. Nefedov, A. Sihvola, S. Maslovski, and C. Simovski, *Waves and Energy in Chiral Nihility*, Journal of Electromagnetic Waves and Applications **17**, 695 (2003).

[147] J. B. Pendry, *A Chiral Route to Negative Refraction*, Science **306**, 1353 (2004).

[148] B. Wang, J. Zhou, T. Koschny, and C. M. Soukoulis, *Nonplanar chiral metamaterials with negative index*, Applied Physics Letters **94**, 151112 (2009).

[149] E. Plum, J. Zhou, J. Dong, V. A. Fedotov, T. Koschny, C. M. Soukoulis, and N. I. Zheludev, *Metamaterial with negative index due to chirality*, Phys. Rev. B **79**, 035407 (2009).

[150] A. Papakostas, A. Potts, D. M. Bagnall, S. L. Prosvirnin, H. J. Coles, and N. I. Zheludev, *Optical Manifestations of Planar Chirality*, Phys. Rev. Lett. **90**, 107404 (2003).

[151] E. Hendry, T. Carpy, J. Johnston, M. Popland, R. Mikhaylovskiy, A. Lapthorn, S. Kelly, L. Barron, N. Gadegaard, and M. Kadodwala, *Ultrasensitive detection and characterization of biomolecules using superchiral fields*, Nat. Nanotechnol. **5**, 783 (2010).

[152] Y. Tang and A. E. Cohen, *Enhanced Enantioselectivity in Excitation of Chiral Molecules by Superchiral Light*, Science **332**, 333 (2011).

[153] T. M. Lowry, *Optical Rotatory Power* (Dover Publications Inc., 1964).

[154] L. D. Barron, *Molecular Light Scattering and Optical Activity* (Cambridge University Press; 2 edition, 2009).

[155] K. Iizuka, *Elements of Photonics Volume 1* (Wiley-Interscience, 2002).

[156] G. R. Fowles, *Introduction to Modern Optics, 2nd edition* (Dover Publications Inc., 1989).

[157] A.-J. Fresnel, , Ann. Chim. Phys. **28**, 147 (1825).

[158] R. D. L. Kronig, *On the Theory of dispersion of X-Rays*, J. Opt. Soc. Am. **12**, 547 (1926).

[159] M. W. Knight and N. J. Halas, *Nanoshells to nanoeggs to nanocups: optical properties of reduced symmetry coreshell nanoparticles beyond the quasistatic limit*, New Journal of Physics **10**, 105006 (2008).

[160] J. B. Pendry, *Negative Refraction Makes a Perfect Lens*, Phys. Rev. Lett. **85**, 3966 (2000).

[161] Z. Liu, S. Durant, H. Lee, Y. Pikus, N. Fang, Y. Xiong, C. Sun, and X. Zhang, *Far-Field Optical Superlens*, Nano Letters **7**, 403 (2007).

[162] X. Chen, L. Huang, H. Muehlenbernd, G. Li, B. Bai, Q. Tan, G. Jin, C.-W. Qiu, S. Zhang, and T. Zentgraf, *Dual-polarity plasmonic metalens for visible light.*, Nat Commun **3**, 1198 (2012).

[163] N. Fang, H. Lee, C. Sun, and X. Zhang, *Sub-Diffraction-Limited Optical Imaging with a Silver Superlens*, Science **308**, 534 (2005).

[164] N. Liu, M. Mesch, T. Weiss, M. Hentschel, and H. Giessen, *Infrared Perfect Absorber and Its Application As Plasmonic Sensor*, Nano Letters **10**, 2342 (2010).

[165] T. Ergin, N. Stenger, P. Brenner, J. B. Pendry, and M. Wegener, *Three-Dimensional Invisibility Cloak at Optical Wavelengths*, Science **328**, 337 (2010).

[166] H. F. Ma and T. J. Cui, *Three-dimensional broadband and broad-angle transformation-optics lens.*, Nat Commun **1**, 124 (2010).

[167] A. Ghosh and P. Fischer, *Chiral Molecules Split Light: Reflection and Refraction in a Chiral Liquid*, Phys. Rev. Lett. **97**, 173002 (2006).

[168] M. C. T. Bahaa E. A. Saleh, *Fundamentals of Photonics 2nd Edition* (Wiley Series in Pure and Applied Optics, 2007).

[169] P. Bharadwaj, B. Deutsch, and L. Novotny, *Optical Antennas*, Adv. Opt. Photon. **1**, 438 (2009).

[170] P. Biagioni, J.-S. Huang, and B. Hecht, *Nanoantennas for visible and infrared radiation*, Reports on Progress in Physics **75**, 024402 (2012).

[171] S. A. Maier, *Plasmonics: Fundamentals and Applications* (Springer, 2007).

[172] Y. Sun, B. Edwards, A. Alu, and N. Engheta, *Experimental realization of optical lumped nanocircuits at infrared wavelengths*, Nat. Mater. **11**, 208 (2012).

[173] A. Alù and N. Engheta, *Input Impedance, Nanocircuit Loading, and Radiation Tuning of Optical Nanoantennas*, Phys. Rev. Lett. **101**, 043901 (2008).

[174] O. Pérez-González, N. Zabala, A. G. Borisov, N. J. Halas, P. Nordlander, and J. Aizpurua, *Optical Spectroscopy of Conductive Junctions in Plasmonic Cavities*, Nano Letters **10**, 3090 (2010).

[175] P. Chen and A. Alù, *Optical nanoantenna arrays loaded with nonlinear materials*, Phys. Rev. B **82**, 235405 (2010).

[176] N. Large, M. Abb, J. Aizpurua, and O. L. Muskens, *Photoconductively Loaded Plasmonic Nanoantenna as Building Block for Ultracompact Optical Switches*, Nano Letters **10**, 1741 (2010).

[177] F. Zhou, Y. Liu, Z.-Y. Li, and Y. Xia, *Analytical model for optical bistability in nonlinear metal nano-antennae involving Kerr materials*, Opt. Express **18**, 13337 (2010).

[178] I. S. Maksymov, A. E. Miroshnichenko, and Y. S. Kivshar, *Actively tunable bistable optical Yagi-Uda nanoantenna*, Opt. Express **20**, 8929 (2012).

[179] E. J. R. Vesseur, *Electron Beam Imaging and Spectroscopy of Plasmonic Nanoantenna Resonances*, Ph.D. thesis, Utrecht University, 2011.

[180] M. Frimmer, T. Coenen, and A. F. Koenderink, *Signature of a Fano Resonance in a Plasmonic Metamolecule's Local Density of Optical States*, Phys. Rev. Lett. **108**, 077404 (2012).

[181] M. Schnell, A. Garcia-Etxarri, A. J. Huber, K. Crozier, J. Aizpurua, and R. Hillenbrand, *Controlling the Near-Field Oscillations of Loaded Plasmonic Nanoantennas*, Nat. Photonics **3**, 287 (2009).

[182] P. Ghenuche, S. Cherukulappurath, T. H. Taminiau, N. F. van Hulst, and R. Quidant, *Spectroscopic Mode Mapping of Resonant Plasmon Nanoantennas*, Phys. Rev. Lett. **101**, 116805 (2008).

[183] H. Fischer and O. J. F. Martin, *Engineering the optical response of-plasmonic nanoantennas*, Opt. Express **16**, 9144 (2008).

[184] W. Zhang, L. Huang, C. Santschi, and O. J. F. Martin, *Trapping and Sensing 10 nm Metal Nanoparticles Using Plasmonic Dipole Antennas*, Nano Letters **10**, 1006 (2010).

[185] A. F. Koenderink, M. Kafesaki, B. C. Buchler, and V. Sandoghdar, *Controlling the Resonance of a Photonic Crystal Microcavity by a Near-Field Probe*, Phys. Rev. Lett. **95**, 153904 (2005).

[186] M. Burresi, T. Kampfrath, D. van Oosten, J. C. Prangsma, S. Song, B. S. Noda, and L. Kuipers, *Magnetic Light-Matter Interactions in a Photonic Crystal Nanocavity*, Phys. Rev. Lett. **105**, 123901 (2010).

[187] M. Burresi, *Nanoscale investigation of ligth-matter interactions mediated by magnetic and electric coupling*, Ph.D. thesis, University of Twente, 2010.

[188] S. Johnson, M. Povinelli, M. Soljacic, A. Karalis, S. Jacobs, and J. Joannopoulos, *Roughness losses and volume-current methods in photonic-crystal waveguides*, Applied Physics B **81**, 283 (2005).

[189] S. G. Johnson, M. Ibanescu, M. A. Skorobogatiy, O. Weisberg, J. D. Joannopoulos, and Y. Fink, *Perturbation theory for Maxwell's equations with shifting material boundaries*, Phys. Rev. E **65**, 066611 (2002).

[190] J. D. Jackson, *Classical Electrodynamics, 3rd Ed.* (John Wiley & Sons, Inc., 1999).

[191] C. Bohren and D. R. Huffman, in *Absorption and Scattering of Light by Small Particles*, edited by C. Bohren and D. R. Huffman (Wiley Science Paperback Series, 1998).

[192] R. Waldron, *Perturbation theory of resonant cavities*, Proc. Inst. Electr.Eng. **107C**, 272 (1960).

[193] O. Klein, S. Donovan, M. Dressel, and G. Grner, *Microwave cavity perturbation technique: Part I: Principles*, Int. J. Infrared Millim. Waves **14**, 2423 (1993).

Summary

The work described in this thesis was shaped by the goal—coming up new approaches to fabricate plasmonic materials with electron beam induced deposition (EBID). One-step, bottom-up and direct-write are typical adjectives that are used to indicate the advantageous properties of this technique. These properties enable us to produce complex, three-dimensional materials even on non-flat substrates in a rapid fashion. However, to fabricate plasmonic materials with EBID one needs to overcome some difficulties and limitations. The major challenge to solve is the impurity issue of the deposited metallic structures. We circumvent the impurity problem by deposition of silica instead of a metal. Metallic nanostructures are obtained by subsequent conformal thin gold film coating. At the end of the coating process we obtain a core-shell type plasmonic structure. With this method, as demonstrated in Chapter 3, we fabricate high aspect ratio ground plane dispersive nanoantennas. The characterization of the structures with angle-resolved cathodoluminescence (CL) and numerical calculations with finite element modeling (FEM) reveal that the nanoantennas work like their rf counterparts, but now in the visible domain and with an effective length that is roughly twice their geometrical length. Furthermore, the core-shell structure of the nanoantennas can be exploited to control and tune the optical properties by altering the shell thickness. In other words the method to circumvent the intrinsic problem of EBID of metals yields an unique advantage for plasmonic structures.

The capacity to build three-dimensional complex structures is a striking feature of EBID. We exploit this feature to fabricate a plasmonic chiral nanoantanna array composed of three-turn helices. The core-shell structure is achieved with the same method that is used to fabricate the ground plane nanoantennas. As described in Chapter 4, we observe that the fabrication process that requires a significant amount of time —like the fabrication of

our helix array— can suffer from a decreased amount of precursor delivery with time. This decrease affects the geometry and size of the individual nanostructures. We circumvent this issue by depositing the helix array part by part with certain amount of pause in between the subsequent depositions. We also observed that, given a fixed replenishment rate of the precursor, electron beam current and dwell time yield different geometries even when the total electron dose is kept constant. In Chapter 5 characterization of the structure is performed with transmission measurements by using circularly polarized light. We demonstrate that our helix array is an optically active material in the visible domain: the transmission depends on the handedness of the circularly polarized light. The results are also supported with numerical calculations.

In Chapter 6 we load the gap of plasmonic split-wire gold nanoantennas with the local deposition feature of EBID. The loading is established with silica deposition. The gap field of the nanoantennas are loaded with various amount of silica. The optical properties of the loaded antennas are investigated with CL spectroscopy. The results reveal that the gap loading shifts the antenna resonance towards longer wavelengths as a function of the amount of deposited silica.

Summarizing, light-matter interaction related studies beyond the classical limits of the optics (nanophotonics) is a broad field. Both fundamental and applied nanophotonics investigations require state-of-the-art nanostructures with various geometries and material properties to push the boundaries. The work in this thesis demonstrates that EBID is an attractive nanofabrication technique to produce nanostructures that are three-dimensional, tunable (active or passive), with different materials, on different types of surface.

Samenvatting*

Het werk beschreven in dit proefschrift is bepaald door het doel Het creëren van nieuwe manieren om plasmonische materialen te fabriceren met behulp van Elektronen Bundel geInduceerde Depositie (EBID). Een-stap, bottom-up en direct-geschreven zijn veelgebruikte termen om de voordelen van deze techniek te beschrijven. Eigenschappen zoals deze stellen ons in staat om snel en zelfs op niet vlakke ondergronden, complexe, driedimensionale structuren te maken. Echter, om plasmonische materialen te kunnen maken met EBID zijn er uitdagingen en beperkingen die overwonnen moeten worden. De grootste beperking is de onzuiverheid van het aangebrachte metaal. Wij gaan deze beperking uit de weg door in eerste instantie silica in plaats van metalen structuren te fabriceren. Vervolgens maken wij deze tot metallische nanostructuren door het silica met een dunne laag goud te bedekken. Het resultaat van dit proces is een kern-schil type plasmonische structuur. Op deze manier fabriceren wij, zoals aangetoond in hoofdstuk 3, geaarde nanoantennes met een hoge verhouding tussen hoogte en dikte. De karakterisering van deze structuren, door middel van hoek-opgeloste kathodoluminescentie (CL) en numerieke berekeningen gebaseerd op Finite Element Modelling (FEM), toont aan dat deze nanoantennes in het zichtbaar spectrum net zo werken als hun evenknieën in het radio spectrum, zij het met een effectieve lengte ruwweg twee keer zo lang als hun geometrische lengte. Bovendien kan de kern-schil structuur van de nanoantennes worden benut om hun optische eigenschappen te controleren door middel van het aanpassen van de dikte van de gouden schil.

De mogelijkheid om driedimensionale complexe structuren te fabriceren is een waardevolle eigenschap van EBID. Wij maken daar gebruik van door een periodieke rangschikking van driedimensionale chirale plasmonische he-

---

*Translated by Boris le Feber

lixen met drie wendingen te maken. De kern-schil structuur is op diezelfde manier gemaakt als de geaarde nanoantennes. Zoals beschreven in hoofdstuk 4 kost het fabricage proces veel tijd; specifiek kan het bemoeilijkt worden afnemende hoeveelheid precursor tijdens het fabricage proces. Deze afname beïnvloedt de vorm en grootte van de individuele antennes. Wij lossen dit probleem op door de periodieke helix rangschikking in delen te fabriceren, met een vaste hoeveelheid tijd tussen de fabricage van de afzonderlijke delen. Bovendien hebben wij ook aangetoond dat indien de afname van de precursor constant in de tijd is, de stroom van de elektronen bundel en de belichtingstijd gebruikt kunnen worden om verschillende vormen helices te fabriceren, zelfs wanneer de elektronen dosis constant gehouden wordt.

In hoofdstuk 5 karakteriseren wij deze helices door middel van transmissie metingen met circulair gepolariseerd licht. Wij tonen aan dat onze periodieke helix rangschikking optisch actief is voor zichtbaar licht: de transmissie hangt af van de oriëntatie van de polarisatie van het licht. Deze metingen worden met numerieke simulaties onderbouwd.

In hoofdstuk 6, vullen wij de opening van plasmonische gouden onderbroken-draad nanoantennes door gebruik te maken van de mogelijkheid van EBID om lokaal materiaal aan te brengen. Op deze manier vullen wij de opening met verschillende hoeveelheden silica. Dit heeft tot gevolg dat de velden in de ruimte tussen de antennes zijn gevuld met verschillende hoeveelheden silica. Wij onderzoeken the optische eigenschappen van deze antennes met CL spectroscopie. De resultaten hiervan laten zien dat de opvulling de resonantie van de antenne naar langere golflengtes verschuift als een functie van de hoeveelheid aangebracht materiaal.

Samenvattend, is de studie naar de wisselwerking tussen licht en materie voorbij de klassieke beperkingen van optica (nanofotonica) is een breed veld. Zowel fundamentele als toegepaste nanofotonica studies vereisen state-of-the-art nanostructuren van verschillende vormen en met verschillende materiaal eigenschappen om hun grenzen te verleggen. Het werk in dit proefschrift toont aan dat EBID een aantrekkelijke nanofabricage techniek is om driedimensionale, controleerbare (zowel actieve als passieve) nanostructuren te fabriceren van verschillende materialen en op verschillende ondergronden.

Acknowledgements

This thesis is established within the FOM-FEI Industrial Partnership Program (IPP). I would like to thank all people who are involved in this joint research program from writing the proposals to the management of this great partnership. I thank to Hans Mulders of FEI for his valuable technical support.

I am sincerely and heartily grateful to my supervisor Prof. L. (Kobus) Kuipers for his guidance and patient support during my whole PhD. Especially, in spite of his busy schedule, I owe thankfulness for his invaluable help during the writing period of this thesis. His sincere personality and encouragement has a remarkable role in the success of this dissertation. I had also a chance to be supervised by Prof. W. Vos for a while when he was at AMOLF. I greatly appreciate his invaluable advices and guidance during his supervision.

I would like to thank the engineers of the Amsterdam NanoCenter, Dimitry Lamers and Johan Derks and Chris Rétif for their significant technical support. I thank to Gijs Vollenbroek for the fabrication of split-wire nanoantennas. My special thanks to Hans Zeijlemaker. His enthusiasm and deep experience were always helpful during my hard times in the NanoCenter.

I wish to thank Prof. A. Polman, the Director of AMOLF, all members of the support and service teams of AMOLF. They shoulder the burden of this institute with a great coherence and has a remarkable role in providing us a comfortable and a convenient research environment.

AMOLF's Center for Nanophotonics is composed of several research groups study on different fields of Nanophotonics. Weekly colloquia and poster-discussion sessions are great opportunity to expand our knowledge beyond the topics studied within our group. From the group leaders to students, I would like to thank all members of the Center for Nano Photonics

for the fruitful discussions and presentations. As the CL technique takes a very important place in the measurement part of this work I would particularly like to thank Toon Coenen for the invaluable collaboration in the CL measurements and I greatly appreciate Prof. A. Polman's thoughtful comments and suggestions regarding the project presented in Chapter 3

It was a great pleasure and opportunity to make science as a member of the NanoOptics Group. I had a chance to work with not only smart but also friendly people here. My special thanks to our group leader Kobus Kuipers, I am sure that every member of the group will not forget his famous 'teaching moments'. He is not only a great scientist but also a good chairman for making an amazing ambiance with balancing the dose of science and fun in the group discussions. I would like to thank Tobias Kamprath, Aron Opheij, Valerian Giesz and Jean Jesario for their help in our optics lab, I thank to Daryl Beggs for his careful reading and checking my manuscripts, Daan Stellinga for his simulation model I benefited for 3D calculations in Chapter 5, Dries van Oosten, Matteo Burresi, Matthias Wulf, Ruben van der Wel, Leon Webbers, Anouk de Hoogh, Nicolaas van der Voort for fruitful discussions. I thank to Hinco Schoenmaker, our super talented technician, for his all kind of technical help related to our setups and workshop jobs. My special thanks to Boris le Feber, the NanoOptics Group's hard working experimentalist and my polite officemate. It was a pleasure to share our office and make discussions not only about science but also sports and other things happening in the world. I am sure that when the time comes he is going to finish his PhD with a great success.

Sevgili anne ve babama ise burada teşekkür adına yazılabilecek herşeyin kifayetsiz kalacağı aşikar. Bundan yıllar önce doktora için geçici bir süre de olsa evden ayrıldığımda ne kadar üzüldüklerini hissedebiliyorum. Bu tezin mevcudiyeti herseye rağmen benden hayır dualarını hiçbir zaman eksik etmemelerinin de bir neticesi olsa gerek. Allah ikisinden de razi olur, rahmetini esirgemez inşallah.

Kıymetli eşim Nur Hanım bu meşakkatli doktora yıllarında bana daima sabırla destek olmuş, doktoramın en sıkıntılı zamanlarında bana sabırla can yoldaşlığı yapmıştır. Sevgili oğlumuzun dünyaya geliş sürecini de sadece benim desteğimle, gurbette geçirmek zorunda kalan sevgili eşime çok az insana nasib olacak olgunluk ve güçlülüğinden dolayı büyük bir teşekkür borçluyum. Allah iki cihanda da mükafatını verir inşallah.